

# Subaru Weak Lensing Measurements of Four Strong Lensing Clusters: Are Lensing Clusters Over-Concentrated?<sup>1</sup>

Masamune Oguri,<sup>2</sup> Joseph F. Hennawi,<sup>3</sup> Michael D. Gladders,<sup>4</sup> Håkon Dahle,<sup>5</sup>  
 Priyamvada Natarajan,<sup>6</sup> Neal Dalal,<sup>7</sup> Benjamin P. Koester,<sup>4,8</sup>  
 Keren Sharon,<sup>4,9</sup> and Matthew Bayliss<sup>4,8</sup>

## ABSTRACT

We derive radial mass profiles of four strong lensing selected clusters which show prominent giant arcs (Abell 1703, SDSS J1446+3032, SDSS J1531+3414, and SDSS J2111–0115), by combining detailed strong lens modeling with weak lensing shear measured from deep *Subaru* Suprime-cam images. Weak lensing signals are detected at high significance for all four clusters, whose redshifts range from  $z = 0.28$  to  $0.64$ . We demonstrate that adding strong lensing information with known arc redshifts significantly improves constraints on the mass density profile, compared to those obtained from weak lensing alone. While the mass profiles are well fitted by the universal form predicted in  $N$ -body simulations of the  $\Lambda$ -dominated cold dark matter model, all four clusters appear to be slightly

---

<sup>1</sup>Based on data collected at Subaru Telescope, which is operated by the National Astronomical Observatory of Japan. Based on observations obtained at the Gemini Observatory, which is operated by the Association of Universities for Research in Astronomy, Inc., under a cooperative agreement with the NSF on behalf of the Gemini partnership: the National Science Foundation (United States), the Science and Technology Facilities Council (United Kingdom), the National Research Council (Canada), CONICYT (Chile), the Australian Research Council (Australia), Ministério da Ciência e Tecnologia (Brazil) and SECYT (Argentina)

<sup>2</sup>Kavli Institute for Particle Astrophysics and Cosmology, Stanford University, 2575 Sand Hill Road, Menlo Park, CA 94025, USA.

<sup>3</sup>Department of Astronomy, University of California Berkeley, Berkeley, CA 94720, USA.

<sup>4</sup>Department of Astronomy & Astrophysics, University of Chicago, Chicago, IL 60637, USA.

<sup>5</sup>Institute of Theoretical Astrophysics, University of Oslo, P.O. Box 1029, Blindern, N-0315 Oslo, Norway.

<sup>6</sup>Department of Astronomy, Yale University, P. O. Box 208101, New Haven CT 06511-208101, USA.

<sup>7</sup>Canadian Institute for Theoretical Astrophysics, 60 St. George Street, University of Toronto, Toronto, ON M5S3H8, Canada.

<sup>8</sup>Kavli Institute for Cosmological Physics, The University of Chicago, Chicago, IL 60637, USA.

<sup>9</sup>School of Physics and Astronomy, Tel-Aviv University, Tel-Aviv 69978, Israel.

more centrally concentrated (the concentration parameters  $c_{\text{vir}} \sim 8$ ) than theoretical predictions, even after accounting for the bias toward higher concentrations inherent in lensing selected samples. Our results are consistent with previous studies which similarly detected a concentration excess, and increases the total number of clusters studied with the combined strong and weak lensing technique to ten. Combining our sample with previous work, we find that clusters with larger Einstein radii are more anomalously concentrated. We also present a detailed model of the lensing cluster Abell 1703 with constraints from multiple image families, and find the dark matter inner density profile to be cuspy with the slope consistent with  $-1$ , in agreement with expectations.

*Subject headings:* dark matter — galaxies: clusters: individual (Abell 1703, SDSS J1446+3032, SDSS J1531+3414, SDSS J2111–0115) — gravitational lensing

## 1. Introduction

The current standard model of structure formation is successful in explaining various cosmological observations, such as the cosmic microwave background (Spergel et al. 2003), the clustering pattern of galaxies (Eisenstein et al. 2005), the Ly $\alpha$  forest fluctuations in the intergalactic medium (McDonald et al. 2005), and the abundance of clusters of galaxies (Gladders et al. 2007; Vikhlinin et al. 2009). In the theory, the growth of structure is driven by the gravitational instability of dark matter. The initial density fluctuations are nearly scale-invariant and Gaussian, as inferred from the cosmic microwave background observations (e.g., Komatsu et al. 2009). The spectrum of the fluctuation, together with the “cold” ansatz of dark matter, suggests that astronomical objects form through the bottom-up assembly process.

Clusters of galaxies serve as one of the most important tests of the standard structure formation model. Clusters are the largest virialized objects in the universe. Their high virial temperatures suggest that most of baryon remain hot in massive clusters and dissipative cooling of baryons is less efficient. Therefore, the density profile of clusters can well be approximated by the distribution of dark matter which is sensitive to both the nature of dark matter and the dark matter assemble history. In the standard collisionless cold dark matter (CDM) scenario, the density profile of dark matter found in  $N$ -body simulations has a universal form with its slope progressively shallower toward the center (Navarro et al. 1997, hereafter NFW). Cluster-scale halos are predicted to have rather low-concentration mass profiles (e.g., Bullock et al. 2001; Neto et al. 2007). These are important theoretical predictions that should be confronted with observations.

Gravitational lensing is suited for this purpose, because it probes the distribution of dark matter directly. Weak gravitational lensing, which takes advantage of small distortions of background galaxies to reconstruct the mass distribution, is particularly powerful in extracting outer mass profiles of massive clusters. On the other hand, strong lensing provides robust measurements of cluster masses near the center. Therefore, it is essential to combine strong and weak lensing analysis in order to constrain density profiles over a wide range of radii (Natarajan et al. 1998, 2002; Bradač et al. 2006, 2008a,b; Diego et al. 2007; Limousin et al. 2007; Hicks et al. 2007; Deb et al. 2008; Merten et al. 2009).

Cluster mass profiles grow in importance, particularly given possible high concentrations found in some lens-rich clusters. Broadhurst et al. (2005a) argued that the radial mass profile of Abell 1689 (A1689) from combined strong and weak lensing analysis appears to be significantly more centrally concentrated than expected from  $N$ -body simulations of dark matter (see also Clowe & Schneider 2001; King et al. 2002; Halkola et al. 2006; Bardeau et al. 2007; Limousin et al. 2007; Umetsu & Broadhurst 2008). Such high concentrations have also been suggested in other lensing clusters, such as CL0024 (Kneib et al. 2003) and MS2137 (Gavazzi et al. 2003). A possible resolution is to consider a triaxial cluster with its major axis aligned with the line-of-sight direction (Oguri et al. 2005; Gavazzi 2005; Corless & King 2007). Because of the lensing bias that lens-rich clusters are more likely to be oriented with the major axis (Hennawi et al. 2007), the high concentration of A1689 can in practice be marginally reconciled with the  $\Lambda$ CDM predictions (Oguri et al. 2005; Hennawi et al. 2007; Oguri & Blandford 2009; Corless et al. 2009). The broad range of apparent concentrations expected in the  $\Lambda$ CDM model, both from the intrinsic scatter of concentrations and from additional scatter due to the projection effect, indicates the need for the statistical study of concentrations using a well-controlled sample of lensing clusters (e.g., Broadhurst et al. 2008).

In this paper, we present new detailed lensing analysis of four clusters. All the clusters are new strong lensing clusters discovered by our survey of giant arcs (Hennawi et al. 2008) using a catalog of massive clusters constructed from the imaging and spectroscopic data of the Sloan Digital Sky Survey (SDSS; York et al. 2000). We exploit wide field-of-view and excellent image quality of the *Subaru* Suprime-cam (Miyazaki et al. 2002) to determine the outer mass profiles of the clusters with weak lensing technique. The derived profiles are combined with strong lensing constraints with redshifts of arcs obtained from the *Gemini* telescope. From the lensing analysis we obtain the radial mass profiles of these clusters, and compare them with the  $\Lambda$ CDM prediction.

The structure of this paper is as follows. We summarize our cluster sample for analysis and follow-up data in §2. Then we perform strong and weak lensing analyses in §3 and

§4, respectively. These results are combined in §5. Our results are summarized in §6. In Appendix A, we discuss the inner density profile of one of our target clusters, Abell 1703, constrained from strong lens modeling. Throughout the paper, we adopt a cosmological model with the matter density  $\Omega_M = 0.26$ , the cosmological constant  $\Omega_\Lambda = 0.74$ , and the dimensionless Hubble constant  $h = 0.72$ .

## 2. Cluster Sample and Follow-up Data

We selected our targets for detailed lensing analysis from our sample of lensing clusters with definitive arcs in the SDSS Giant Arc Survey (SGAS; Hennawi et al. 2008). The cluster lens sample has been constructed as follows. We take advantage of a sample of the richest clusters from the 8000 deg<sup>2</sup> photometric data of the SDSS using a red-sequence cluster finding algorithm (Gladders & Yee 2000, 2005). We then obtained follow-up images of the richest clusters with the Wisconsin Indiana Yale NOAO (WIYN) 3.5m telescope, the University of Hawaii 88-inch telescope (UH88), and the Nordic Optical Telescope (NOT), and checked the images visually to locate new giant arcs. Thus the SGAS probes the comoving volume of  $\sim 6 \text{ Gpc}^3$ , representing the largest giant arc survey conducted to date. Although the survey is still ongoing, it has already uncovered more than 30 new lensing clusters that exhibit giant arcs. See Hennawi et al. (2008) for more details on the survey method and initial results of the SGAS.

In this paper, we study the following four clusters; Abell 1703 (hereafter A1703,  $z = 0.281$ ), SDSS J1446+3032 (SDSS1446,  $z = 0.464$ ), SDSS J1531+3414 (SDSS1531,  $z = 0.335$ ), and SDSS J2111–0115 (SDSS2111,  $z = 0.637$ ). Giant arcs of all the four clusters were newly discovered by our survey (Hennawi et al. 2008). Limousin et al. (2008), Saha & Read (2009), and Richard et al. (2009) conducted strong lensing analysis of A1703 based on the *Hubble Space Telescope* images. Broadhurst et al. (2008) presented results of mass modeling of A1703 from both strong and weak lensing. Besides these, no lensing analysis has been published for these clusters.

### 2.1. Imaging Follow-up

We conducted imaging observations of these clusters with the Suprime-Cam (Miyazaki et al. 2002) on the Subaru 8.2-meter telescope on 2007 June 15. It covers a field of view  $\sim 34' \times 27'$  with the pixel scale of  $0''.202$ . For each cluster, we obtained deep  $g$ -,  $r$ -, and  $i$ -band images. We assign longer exposure time to  $r$ -band images because we conduct weak lensing analysis

using  $r$ -band images. The  $g$ - and  $i$ -band images are taken to study colors of strong lens candidates and to select galaxies for shear measurements. We summarize the exposure time, the seeing size, and the limiting magnitude of each image in Table 1. The imaging data are reduced using SDFRED (Yagi et al. 2002; Ouchi et al. 2004). The photometric calibration is performed using the SDSS data by comparing magnitudes of stars between SDSS and Subaru images. Astrometric calibration is performed using reference objects in the USNO-A2.0 catalog. The resulting astrometric accuracy is  $\sim 0''.4$ . We construct object catalogs for these images using SExtractor (Bertin & Arnouts 1996). In this paper we use either total (MAG\_AUTO) or aperture (MAG\_APER with an aperture diameter of  $2''$ ) magnitude. All the magnitudes are corrected for Galactic extinction (Schlegel et al. 1998).

## 2.2. Spectroscopic Follow-up

Spectroscopic observations were conducted for three of the four clusters studied in this paper. SDSS1446, SDSS1531, and SDSS2111 were observed with the Frederick C. Gillett Telescope (Gemini North) between the months of 2008 February and 2008 July. The primary goal of the spectroscopic observations was to obtain redshifts of arcs to facilitate strong lensing modeling. We briefly summarize the spectroscopy here, and refer the reader to Hennawi et al. (2009, in preparation) for additional details.

All spectroscopic observations were carried out using the Gemini Multi-Object Spectrograph (GMOS; Hook et al. 2004) using multi-object slitmasks in microslit nod-and-shuffle (N&S) mode (e.g., Glazebrook & Bland-Hawthorn 2001; Abraham et al. 2004). Custom slitmasks were designed and arcs were targeted based on their colors in the deep Subaru imaging. After targeting all of the arc candidates, any remaining slits were placed on cluster members, easily identified by their red sequence colors.

Spectra were taken with the R150\_G5306 grating in first order which gives a dispersion of  $3.5 \text{ \AA}$  per pixel, with six pixels per resolution element resulting in a spectral FWHM  $\simeq 940 \text{ km s}^{-1}$ . Although the R150 grating offers broad spectral range from the atmospheric cutoff to  $\lambda \gtrsim 1 \mu\text{m}$ , the drop in sensitivity at the blue and red extremes, due both to the GMOS CCD and the R150 grating efficiency, results in effective spectral coverage of  $4000 - 9500 \text{ \AA}$ . Our exposure times were 2400 sec resulting in 1200 sec effective integration for each of the two submasks. Three exposures were taken for each target. Thus if an arc was targeted on both submasks (typical for the most prominent arcs) the total integration time was 7200 sec.

### 3. Strong Lensing Analysis

#### 3.1. Data

We obtain strong lensing constraints of the clusters by fitting the positions of arcs. Figure 1 presents the *Subaru* Suprime-cam images of the central regions of the clusters. As shown in Hennawi et al. (2008), these clusters exhibit clear giant arcs. We identify multiple images based on their colors, redshifts, and also iteratively by building preliminary mass models of the clusters. For A1703, we adopt the identification and spectroscopic redshifts of arcs reported by Limousin et al. (2008) and Richard et al. (2009). The redshifts of giant arcs of SDSS1531 were successfully measured with the *Gemini* telescope. Although we could not measure the redshift of the lensed blue images in SDSS1446 from our *Gemini* spectrum, the absence of [OII] 3727Å emission line and the brightness of the arc in the *g*-band image suggests that the redshift should be in the range  $1.6 < z < 3.5$  (Hennawi et al. 2009, in preparation). We adopt this redshift range in our mass modeling. Since the spectrum of the giant arc of SDSS2111 was inconclusive, we conservatively assume its redshift to be  $z < 3.5$  based on the *g* – *r* color. Although some additional possible multiply imaged systems are identified in some of these clusters, we conservatively restrict our analysis to those image systems where lensing hypothesis is completely unambiguous. We summarize the locations and redshifts of the multiply imaged systems for strong lens modeling in Table 2.

#### 3.2. Mass Modeling

We model the dark matter distribution in each clusters by the NFW profile:

$$\rho(r) = \frac{\rho_s}{(r/r_s)(1 + r/r_s)^2}, \quad (1)$$

where  $\rho_s$  is a characteristic density and  $r_s$  is a scale radius. Throughout the paper, we adopt the virial overdensity  $\Delta_{\text{vir}}(z)$  to compute the virial mass  $M_{\text{vir}}$  and virial radius  $r_{\text{vir}}$ :

$$M_{\text{vir}} = \frac{4}{3}\pi r_{\text{vir}}^3 \Delta_{\text{vir}}(z) \bar{\rho}(z) = \int_0^{r_{\text{vir}}} 4\pi r^2 \rho(r) dr, \quad (2)$$

where  $\bar{\rho}(z)$  is the mean matter density of the universe at redshift  $z$ . The nonlinear overdensity  $\Delta_{\text{vir}}(z)$  is calculated at each  $z$  in a standard way using the spherical collapse model. The concentration parameter  $c_{\text{vir}}$  of the model is defined by

$$c_{\text{vir}} = \frac{r_{\text{vir}}}{r_s}. \quad (3)$$

Thus clusters with larger values of  $c_{\text{vir}}$  are more centrally concentrated.  $N$ -body simulations based on the  $\Lambda$ CDM model predict that concentration parameters depend on halo masses and redshifts; for massive clusters, they are typically  $\sim 5$  at  $z = 0$  and evolve with the redshift as  $(1+z)^{-\alpha}$  with  $\alpha \sim 0.7 - 1$  (Bullock et al. 2001; Wechsler et al. 2002; Zhao et al. 2003; Hennawi et al. 2007; Neto et al. 2007; Duffy et al. 2008; Maccio' et al. 2008).

To compute lensing properties, we first project the spherical NFW profile (eq. [1]) onto a two-dimensional lens plane. Next we include an ellipticity  $e$  by replacing the radius  $r = \sqrt{x^2 + y^2}$  in the projected mass density to  $\sqrt{(1-e)x^2 + y^2/(1-e)}$ . Then we allow an arbitrary position angle  $\theta_e$  by rotating the projected mass density. The lensing deflection angle for our mass profile is computed using the method described in Schramm (1990). Since the ellipticity is introduced in the surface mass density rather than the lens potential, our model does not suffer from unphysical mass distributions (such as dumbbell-like isodensity contours and negative mass densities), which may be seen in the case of elliptical lens potentials (e.g., Golse & Kneib 2002).

We also include member galaxies in our mass modeling. The total mass distribution of each member galaxy is modeled by the pseudo-Jaffe (1983) model which has the three-dimensional radial profile of  $\rho \propto r^{-2}(r^2 + r_{\text{cut}}^2)^{-1}$ , i.e., the isothermal model with the truncation at  $r_{\text{cut}}$ . We identify red member galaxies in the color-magnitude ( $g-i$  versus  $r$ ) diagram and include  $\sim 40$  brightest member galaxies for the mass model of each cluster. We fix the locations, ellipticities, and position angles of the members to those measured in the *Subaru* Suprime-cam data. Note that including the central galaxies is important for accurate estimates of dark matter core masses, as their effects on strong lensing can be significant (e.g., Meneghetti et al. 2003; Hennawi et al. 2007; Wambsganss et al. 2008). On the other hand, the effect of other member galaxies is rather minor, but they can be important in accurately reproducing positions of some lensed images.

To reduce the number of parameters, we adopt the exact scaling relations for the velocity dispersions  $\sigma$  and cutoff radii  $r_{\text{cut}}$  of member galaxies following Natarajan & Kneib (1997), who constrained the mass distribution around cluster elliptical galaxies using detailed strong and weak lensing models. Specifically, we assume that they scale as  $\sigma \propto L^{1/4}$  (Faber-Jackson relation) and  $r_{\text{cut}} \propto L^{1/2}$  (corresponding to a constant mass-to-light ratio), where  $L$  is a total  $r$ -band luminosity of the galaxy. We apply this scaling relation to all member galaxies including the BCG of the cluster. To avoid unrealistically massive member galaxies, we add a Gaussian prior to the normalization of the scaling for the velocity dispersion, which is estimated using the correlation with the magnitude (Bernardi et al. 2003), but we adopt a conservative 20% error so that a wide range of mass models are allowed. We also estimate the normalization of the scaling for the cutoff radius by that inferred from

observations,  $r_{\text{cut}} = 18(\sigma/200\text{km s}^{-1})^2$  kpc (where we fix  $\sigma$  in this relation to the mean normalization of the Gaussian prior on  $\sigma$ ) (Natarajan et al. 2002, 2009), but again allow  $r_{\text{cut}}$  to be Gaussian-distributed with a 50% error which crudely models the uncertainty of this relation in observations.

Finding multiple images for a given source position requires intensive search in the image plane. This is time-consuming, even if we adopt adaptive-mesh refinement scheme to improve grid resolutions only near the critical curves, preventing us from exploring a large parameter space in a reasonable time scale. Instead, in this paper we evaluate  $\chi^2$  in the source plane to speed up (e.g., Kochanek 1991):

$$\chi_{\text{src}}^2 = \sum_i \frac{|\mu_i(\mathbf{u}_i - \mathbf{u}_{\text{src}})|^2}{\sigma_{\text{pos}}^2} + \text{prior}, \quad (4)$$

where  $\mu_i$  is the magnification tensor for observed  $i$ -th image,  $\mathbf{u}_i$  are the source position computed from the position of the  $i$ -th image, and  $\mathbf{u}_{\text{src}}$  is the best-fit source position which can be found analytically (see Keeton 2001). Since the magnification tensor is nothing but a mapping from the source plane to the image plane,  $|\mu_i(\mathbf{u}_i - \mathbf{u}_{\text{src}})|$  approximates the distance between observed and predicted image positions in the image plane; indeed, we confirmed that this source plane  $\chi^2$  is reasonably accurate at around our best-fit models, compared with the standard image plane  $\chi^2$ . Note that this approach automatically ignores any extra images. An important parameter here is the positional uncertainty in the image plane,  $\sigma_{\text{pos}}$ , which is directly related with errors on best-fit model parameters. While the measurement error was sufficiently small, comparable to the pixel scale of the image ( $\sim 0''.2$ ), it has been known that multiple images can be fitted only with  $\sim 1''$  accuracy for some massive lensing clusters (e.g., Broadhurst et al. 2005b), presumably because of complex nature of cluster mass distributions. Thus, in this paper we assume the positional error of  $1''.2$  (image plane) for all multiple images.

We explore the multi-dimensional  $\chi^2$  surface using a Markov chain Monte Carlo (MCMC) approach. We adopt a standard Metropolis-Hastings sampling with the multivariate-Gaussian as a proposal distribution. During the sampling, the range of the virial mass is restricted to  $1.4 \times 10^{14} M_{\odot} < M_{\text{vir}} < 7 \times 10^{15} M_{\odot}$ , and that of the concentration parameter to  $c_{\text{vir}} < 40$ . We then derive constraints on parameters by projecting the likelihood distributions to the parameter space. Mass modeling is performed using the software *glafic* (M. Oguri, in preparation).



### 3.3. Result of Strong Lens Modeling

Results of our strong lens modeling are summarized in Table 3, and the critical curves of the best-fit models are displayed in Figure 1. First, we find that our best-fit models successfully reproduce the multiple images with reduced chi-squares of  $\chi^2/\text{dof} \lesssim 1$ , which suggests that our assumption of the positional error of  $1''.2$  was reasonable. Second, strong lensing constrains the center of the dark halo component quite well with a typical error of an arcsecond, and the best-fit dark halo center is close to the position of the BCG. An exception is SDSS2111 for which the offset of the center of the dark halo from the BCG is large,  $> 10''$  (see below). Third, it is found that the virial mass  $M_{\text{vir}}$  and concentration parameter  $c_{\text{vir}}$  are not constrained very well. In fact this is expected, because multiple images of a source redshift mainly constrain the mass enclosed by the arcs, which is sensitive both to  $M_{\text{vir}}$  and  $c_{\text{vir}}$ . Fourth, we find that relatively large ellipticities of  $e \sim 0.4$  are required to fit the images. An exception is SDSS1531 for which the mass distribution appears to be rather circular,  $e \sim 0.1$ , although an ellipticity as high as  $\sim 0.5$  is allowed. These large ellipticities are in fact broadly consistent with  $\Lambda\text{CDM}$  predictions (e.g., Oguri & Blandford 2009).

Our best-fit mass model of A1703 from strong lensing (see also Appendix A) appears to be in reasonable agreement with earlier work (Limousin et al. 2008; Saha & Read 2009; Richard et al. 2009). For example, best-fit ellipticity and position angle of dark halo component,  $e = 0.36$  and  $\theta_e = -24.1$ , agree well with the result of Richard et al. (2009), the ellipticity in the lens potential of  $e_{\text{pot}} = 0.23$  and  $\theta_e = -26.0$ . (see, e.g., Golse & Kneib 2002, for the relation between  $e_{\text{pot}}$  and  $e$ ). Moreover, we find that the structure of the critical curve of A1703 is consistent with those found in the earlier work. It is worth noting that the central ring (A1–A4) represents a rare example of lensing by a hyperbolic umbilic catastrophe.

One of the most important quantities that are well constrained by strong lensing is the Einstein radius,  $\theta_{\text{Ein}}$ . We obtain constraints on  $\theta_{\text{Ein}}$  at the redshifts of the arcs from our strong lens modeling as follows. For all the MCMC samples we estimate the Einstein radii of the dark halo (NFW) components by forcing  $e = 0$  and calculating the radii of the outer critical curves predicted by the dark halo components alone. Thus the contribution of cluster member galaxies including the central galaxy is removed in our estimate of  $\theta_{\text{Ein}}$ , suggesting that the value could in fact be smaller than observed distances of lensed images from the center. We emphasize that this quantity serves as a useful strong lens constraint when combined with weak lensing results, particularly because we are interested in the radial profile of the dark matter component, rather than the total matter including stars which dominate at the very center of clusters (see §5). The derived constraints on  $\theta_{\text{Ein}}$  are shown in Table 4. Since multiple strong lens systems with different redshifts are available for A1703,

for this particular cluster we derive Einstein radii at two different source redshifts,  $z = 0.8889$  (the redshift of arc A1–A5) and 2.627 (the redshift of arc B1–B3 and C1–C3). We regard these two Einstein radii as statistically independent, which is reasonable given the large difference of  $\theta_{\text{Ein}}$  between these two redshifts.

Here we briefly discuss the mass model of SDSS2111, which appears to exhibit the large offset between the lens potential center and the location of the BCG (see Figure 1; the best-fit lens potential center corresponds to the center of the inner critical curve). We find that no acceptable lens model has the offset smaller than  $\sim 5''$ . The offset is required because the center of curvature of the long bright arc is clearly displaced from the BCG. However, as seen in Table 3, the current data do not constrain the center of the dark halo (NFW) component very well, which is the main reason that  $\theta_{\text{Ein}}$  involve relatively large errors. Thus it is important to improve the strong lens constraints by adding more multiply imaged systems.

## 4. Weak Lensing Analysis

### 4.1. Distortion Measurements

We derive weak lensing shear signals following the algorithm outlined in Kaiser et al. (1995, hereafter KSB). First, for each cluster we reprocess *Subaru* Suprime-cam *r*-band images through IMCAT<sup>1</sup> to compute shapes of each objects. In order to compute shapes accurately, we iteratively refine the centroid of each object. During the process objects with offsets in each iteration larger than 3 pixel are removed. The ellipticities  $\mathbf{e}$  of objects are measured from the weighted quadruple moments of the surface brightnesses. We select stars for Point Spread Function (PSF) correction in a standard way by identifying the stellar branch in the magnitude versus half light radius  $r_h$  plane. We apply an additional cut, the signal-to-noise ratio  $\nu > 15$  and the ellipticity  $|\mathbf{e}| < 0.1$ , to construct a final sample of template stars for the PSF correction. We correct ellipticities of objects using the sample of stars as reference

$$\mathbf{e}_{\text{cor}} = \mathbf{e} - P_{\text{sm}}\mathbf{q}^*, \quad (5)$$

where  $P_{\text{sm}}$  is the smear polarizability tensor and  $\mathbf{q}^* = (P_{\text{sm}}^*)^{-1}\mathbf{e}^*$  is the PSF anisotropy kernel estimated from the template stars (hereafter the superscript \* denotes quantities measured for template stars). Following Okabe & Umetsu (2008) and Umetsu & Broadhurst (2008), we obtain a smooth map of  $\mathbf{e}^*$  by first dividing the whole image into  $5 \times 4$  chunks and fit  $\mathbf{e}^*$

---

<sup>1</sup><http://www.ifa.hawaii.edu/~kaiser/imcat/>

in each chunk using second-order bi-polynomials with iterative  $3\sigma$ -clipping rejections. We show ellipticities of the template stars before and after the PSF correction in Figure 2 and Table 5. The Figure demonstrates that our procedure successfully reduces PSF anisotropies over the entire field. Residual stellar ellipticities after the PSF correction are comparable to those in other weak lensing studies using *Subaru* Suprime-cam images (Hamana et al. 2003; Miyazaki et al. 2007; Okabe & Umetsu 2008; Umetsu & Broadhurst 2008).

Next we correct the isotropic smearing effect to estimate weak lensing shear. The pre-seeing shear polarizability  $P_g$  relates observed galaxy ellipticities with their true values, and is calculated as

$$P_g = P_{\text{sh}} - P_{\text{sm}}(P_{\text{sm}}^*)^{-1}P_{\text{sh}}^*, \quad (6)$$

where  $P_{\text{sh}}$  is the shear polarizability tensor. Since the measurement of  $P_g$  for each galaxy is extremely noisy, we approximate  $P_g$  as  $P_g^s$  times an identity matrix with (Erben et al. 2001; Hettterscheidt et al. 2007):

$$P_g^s = \frac{1}{2} \left\{ \text{tr}(P_{\text{sh}}) - \frac{\text{tr}(P_{\text{sh}}^*)}{\text{tr}(P_{\text{sm}}^*)} \text{tr}(P_{\text{sm}}) \right\}. \quad (7)$$

Here we use a smooth map of  $\text{tr}(P_{\text{sh}}^*)/\text{tr}(P_{\text{sm}}^*)$  constructed by fitting them with a fifth-order polynomial over the entire template stars. We then derive the reduced shear  $\mathbf{g} = \boldsymbol{\gamma}/(1 - \kappa)$  for each object as

$$\mathbf{g} = f_{\text{cal}} \frac{\mathbf{e}_{\text{cor}}}{P_g^s}. \quad (8)$$

We use raw, unsmoothed  $P_g^s$  because the smoothing does not necessarily improve the shear estimate (e.g., Erben et al. 2001). We include the calibration correction factor  $f_{\text{cal}} = 1/0.88$  since the KSB algorithm with the scalar correction scheme for  $P_g$  has been known to underestimate shears by  $\sim 10 - 15\%$  (Erben et al. 2001; Heymans et al. 2006; Massey et al. 2007). We confirmed that our shear estimate procedure, together with the source galaxy selection described in §4.2, recovers lensing shears in the simulated *Subaru* Suprime-cam images of the Shear Testing Programme 2 (STEP2; Massey et al. 2007) quite well, with typically a few percent of the shear-calibration bias (parameter  $m$ ) and an order of magnitude smaller residual shear offset (parameter  $c$ ).

## 4.2. Source Galaxy Population

The background galaxy selection is crucial for weak lensing analysis. We choose following galaxies for weak lensing analysis; (1) no close companions at distances within 10 pixels, (2) the half light radius  $r_h$  larger than  $1.2\overline{r_h^*}$ , where  $\overline{r_h^*}$  is the median of the half light radii of

template stars used for the PSF correction, (3) the half-light radius  $r_h$  smaller than 10 pixels, (4) the signal-to-noise ratio  $\nu > 7$ , (5) the pre-seeing shear polarizability  $P_g^s > 0.05$ , and (6) the shear value  $|\gamma| < 2.0$ . In addition, we apply magnitude and color cuts, as we will discuss below.

An appropriate color selection is important to minimize the dilution effect by cluster member galaxies (e.g., Medezinski et al. 2007). One way to avoid contaminations from cluster members is to use galaxies redder than the red sequence of the cluster or bluest galaxies. In this paper we adopt blue galaxies, because our clusters are located at moderately high redshifts ( $z \sim 0.3 - 0.7$ ) and hence very few red background galaxies are available. Specifically, we use galaxies with  $g - i < 1.0$  (measured in aperture magnitudes) for our weak lensing analysis. This is much bluer than red-sequence galaxies ( $g - i \sim 1.7 - 2.8$  for  $r \sim 24$ ), suggesting that the dilution effect is not significant for our source galaxy samples.

We now estimate the depths of our galaxy sample for weak lensing analysis. A key quantity here is the mean lensing depth averaged over the population of source galaxies:

$$\left\langle \frac{d_{ls}}{d_{os}} \right\rangle = \int dz \frac{dp_{wl}}{dz} \frac{d_{ls}}{d_{os}}, \quad (9)$$

with  $d_{ls}$  and  $d_{os}$  being angular diameter distances from the lens to the source and from the observer to the source, respectively. The PDF  $dp_{wl}/dz$  denotes the redshift distribution of the source galaxy sample, which is particularly important in our study because of relatively high redshifts of the clusters.

To estimate  $dp_{wl}/dz$ , we adopt a photometric redshift sample of galaxies in the Canada-France Hawaii Telescope Legacy Survey (CFHTLS) presented by Ilbert et al. (2006). The idea is that we apply our color and magnitude cuts to the CFHTLS galaxy sample, which is well calibrated by the large amount of photometric and spectroscopic data, to infer the redshift distribution in our *Subaru* galaxy sample. First, we compare the number counts of galaxies with  $g - i < 1.0$  between the CFHTLS and our source galaxy samples. Figure 3 shows the relative weight as a function of total  $r$ -band magnitudes,  $w(r) \propto n_{\text{Subaru}}(r)/n_{\text{CFHTLS}}(r)$ , i.e., the number ratio of the source galaxies and CFHTLS galaxies. Sharp declines at  $r \sim 25$  imply that the effect of our background galaxy selections is significant beyond this magnitude. We therefore use galaxies with total  $r$ -band magnitudes  $22 < r < r_{\text{max}}$  for our weak lensing analysis, where  $r_{\text{max}}$  is chosen so that the relative weight becomes approximately 0.3 (see Table 6 for exact values). Next we estimate the probability distribution functions (PDFs) of redshifts for our background samples  $dp_{wl}/dz$  as

$$\frac{dp_{wl}}{dz} = \frac{\sum w(r) dp/dz(r)}{\sum w(r)}, \quad (10)$$

where the summations run over all CFHTLS galaxies with  $g-i < 1.0$  and  $22 < r < r_{\max}$ , and  $dp/dz(r)$  is the PDFs of photometric redshifts for individual CFHTLS galaxies (Ilbert et al. 2006). With this PDF, we estimate the lensing depths  $\langle d_{ls}/d_{os} \rangle$  from equation (9).

Table 6 summarizes the mean depths of our source galaxy sample. We also compute the effective source redshift  $z_d$  that is defined by the redshift at which the distance ratio  $d_{ls}/d_{os}$  becomes equal to the mean distance ratio  $\langle d_{ls}/d_{os} \rangle$ ; in most situations of weak lensing analyses we can simply assume that all the source galaxies lie at  $z = z_d$ . However, since the reduced shear  $\mathbf{g} = \gamma/(1 - \kappa)$  is not exactly proportional to  $d_{ls}/d_{os}$ , adopting a common redshift for all background galaxies in fact underpredicts values of  $\mathbf{g}$  (Seitz & Schneider 1997; Hoekstra et al. 2000). Thus, in computing expected  $\mathbf{g}$  for a given mass model we fully take account of the redshift distribution of background galaxies  $dp_{wl}/dz$  instead of adopting the effective source redshift  $z_d$ .

The resulting numbers of background galaxies are  $\sim 9000 - 10000$  (surface number density of  $n_g \sim 10 \text{ arcmin}^{-2}$ ), except SDSS1531 for which the number of source galaxies is much smaller,  $\sim 6000$  ( $n_g \sim 7 \text{ arcmin}^{-2}$ ), because of the worse seeing size of the image. The reason for the relatively small number density compared with the expected number density of  $n_g \sim 30 - 40 \text{ arcmin}^{-2}$  for *Subaru* weak lensing (e.g., Miyazaki et al. 2007) is our color cut to eliminate the dilution effect. In fact, the number density is comparable to other *Subaru* cluster weak lensing studies which adopted similar color cuts (e.g., Okabe & Umetsu 2008).

### 4.3. Two-Dimensional Mass Distributions

Before studying radial profiles, we check two-dimensional mass (convergence) distributions reconstructed from weak lensing shears using an inversion algorithm of Kaiser & Squires (1993) and assuming weak lensing limit ( $\kappa \ll 1$ ). We use these two-dimensional mass maps only to study the morphology of the cluster; we constrain cluster mass distributions using radial profiles of tangential shears (see §4.4). We also derive luminosity density maps of red-sequence galaxies for comparison.

We show Gaussian-smoothed ( $\sigma = 60''$ ) maps of all four clusters in Figure 4. In all the clusters, weak lensing signals are clearly detected. In addition, we find that the reconstructed mass distributions well trace the spatial distributions of red-sequence galaxies, with roughly similar mass and light centroids. The clusters exhibit deviations from circular mass distributions, in particular for A1703. The agreement of position angles from weak lensing, the light distribution, and strong lensing (see the critical curve shown in Figure 1) implies that the cluster A1703 is quite relaxed. For SDSS1531, we find a probable secondary peak at the

$\sim 4'$  northwest of the cluster center, implying that the cluster may not yet be relaxed. The position angles of mass distributions from strong and weak lensing appear to agree. Several subpeaks and non-regular morphology of SDSS2111 suggest that this cluster is not relaxed either. However, SDSS2111 again shows agreement between weak and strong lensing in that the isodensity contours appear to be elongated in the north-south direction. In addition, the centroid of the mass distribution is slightly offset North of the BCG, which is consistent with the result of strong lens modeling.

#### 4.4. Tangential Shear Profiles

For each cluster we derive an azimuthally averaged one-dimensional shear profile to obtain constraints on the cluster mass profiles. The center of each cluster is fixed to the center of the dark halo component determined from strong lens modeling (see Table 3). For a given center, we can calculate the tangential shear  $g_+$  and the  $45^\circ$  rotated component  $g_\times$  from the reduced shear  $\mathbf{g} = (g_1, g_2)$  as follows:

$$g_+ = -g_1 \cos 2\phi - g_2 \sin 2\phi, \quad (11)$$

$$g_\times = -g_1 \sin 2\phi + g_2 \cos 2\phi, \quad (12)$$

where  $\phi$  is the polar angle. We obtain  $g_+$  and  $g_\times$  for each radial bin by simply averaging these shears of individual source galaxies without weighting. We estimate the mean and error using a jackknife resampling technique. The shear profiles are computed in the range of radii  $\theta = [0'.8, 20']$  with a bin size of  $\Delta \log \theta = 0.2$ . Thus we have seven radial bins in total.

In Figure 5, we plot radial profiles of  $g_+$  and  $g_\times$  of all the four clusters. We detect weak lensing signals significantly up to  $\sim 10'$  from the cluster center. On the other hand,  $g_\times$  is consistent with a null signal, as expected for shears produced by gravitational lensing of clusters. We fit the tangential shear profile by the NFW profile (eq. [1]) with the virial mass  $M_{\text{vir}}$  and concentration parameters  $c_{\text{vir}}$  as free parameters. For this, we adopt the following  $\chi^2$ :

$$\chi_{\text{WL}}^2 = \sum_i \frac{[\bar{g}_{+,i} - g_+(\theta_i; M_{\text{vir}}, c_{\text{vir}})]^2}{\sigma_i^2}, \quad (13)$$

where  $\bar{g}_{+,i}$  and  $\sigma_i$  denote observed tangential shear and its error for  $i$ -th radial bin. As shown in Figure 5, the NFW model provides reasonable fits to the data. The best-fit model parameters are summarized in Table 7.

## 5. Combining Strong and Weak Lensing

### 5.1. Constraints on Parameters

In this section, we combine results from strong lensing (§3) and weak lensing (§4) to constrain the radial mass profiles over a wide range of radii. We do so simply by summing up the chi-squares:

$$\chi^2 = \chi_{\text{SL}}^2 + \chi_{\text{WL}}^2, \quad (14)$$

where the weak lensing constraint  $\chi_{\text{WL}}^2$  is from equation (13). Although we can in principle use strong lens constraints obtained from detailed fitting of image positions in §3, here we choose a conservative approach to adopt only the Einstein radius as our strong lens constraint. Specifically,  $\chi_{\text{SL}}^2$  is computed as

$$\chi_{\text{SL}}^2 = \sum \frac{[\bar{\theta}_{\text{Ein}} - \theta_{\text{Ein}}(M_{\text{vir}}, c_{\text{vir}})]^2}{\sigma_{\text{Ein}}^2}, \quad (15)$$

where  $\bar{\theta}_{\text{Ein}}$  and  $\sigma_{\text{Ein}}$  are the Einstein radius and its errors listed in Table 4. We include the asymmetry of errors on  $\bar{\theta}_{\text{Ein}}$  by using different values of  $\sigma_{\text{Ein}}$  between  $\theta > \bar{\theta}_{\text{Ein}}$  and  $\theta < \bar{\theta}_{\text{Ein}}$ . For SDSS1446 and SDSS2111, only the allowed range of the redshift of the arcs (and hence the redshift of the Einstein radius,  $z_{\text{Ein}}$ ) was given; therefore, for these clusters we assume a flat prior  $1.6 < z_{\text{Ein}} < 3.5$  (SDSS1446) or  $z_{\text{Ein}} < 3.5$  (SDSS2111) and marginalize  $\chi_{\text{SL}}^2$  over  $z_{\text{Ein}}$  to derive strong lens constraints. We note that the contribution of stars (member galaxies and the BCGs), which can be significant at strong lensing regime, is excluded in estimating  $\theta_{\text{Ein}}$  from strong lens modeling. Thus the derived radial profile should be considered as that for the sum of dark matter and intracluster gas rather than the total matter profile.

We show the constraints in the  $M_{\text{vir}}\text{-}c_{\text{vir}}$  plane in Figure 6. As expected, adding strong lensing significantly improve constraints on these parameters, especially the concentration parameter  $c_{\text{vir}}$ , although this is not the case for SDSS2111 because of the unknown arc redshift and the relatively large error on  $\theta_{\text{Ein}}$ . Constraints from strong and weak lensing are consistent with each other, except A1703 for which the best-fit models slightly differ. We list the best-fit model parameters in Table 7. It is found that the radial profiles are fitted well by the NFW profile with  $\chi^2/\text{dof} \sim 1$ .

To see how strong and weak lensing probe different radii, we plot radial profiles of convergence  $\kappa$  from lensing observations and best-fit models in Figure 7. We derive convergence at each radial bin from weak lensing shears by using the following relation:

$$g_+(\theta) [1 - \kappa(\theta)] = \frac{2}{\theta^2} \int_0^\theta \theta' \kappa(\theta') d\theta' - \kappa(\theta). \quad (16)$$

We need a boundary condition in order to solve this equation. We fix  $\kappa$  in the outermost bin to the value computed from the NFW profile with best-fit parameter values from weak lensing data alone. See, e.g., Umetsu & Broadhurst (2008) for practical procedures to compute  $\kappa$  from discrete  $g_+$  data. As clearly shown in the Figure, strong lensing probes radii roughly an order of magnitude smaller than those constrained by weak lensing. Hence by combining strong and weak lensing we can constrain the density profile of the cluster over 2 dex in radius. We find that the model that fits weak lensing data of A1703 underpredicts convergence in the core of the cluster; the Einstein radius of A1703 implies more centrally concentrated profile of A1703 than expected from weak lensing data alone. For the other three clusters, convergence profiles from weak lensing alone and strong and weak lensing agree quite well. However, strong lensing data do narrow down the allowed range of radial profiles, as is clear from Figure 6.

We now compare our result of A1703 with the combined strong and weak lensing analysis by Broadhurst et al. (2008). We find that the best-fit virial masses are consistent with each other, but the concentration parameter of our best-fit model,  $c_{\text{vir}} = 6.5_{-0.7}^{+1.2}$ , differs from their best-fit value,  $c_{\text{vir}} = 9.9_{-1.6}^{+2.4}$  at  $\sim 2\sigma$  level. We ascribe the difference to the larger Einstein radius they assumed,  $\theta_{\text{Ein}} = 33''$  for  $z_s = 2.8$ . Indeed, our best-fit model predicts  $\theta_{\text{Ein}} = 22''$  for  $z_s = 2.8$ , which appears more consistent with the locations of lensed arcs in A1703 (see also Richard et al. 2009).

## 5.2. Distribution of the Concentration Parameter

One of our main interests lies in the possible excess of the concentration parameter  $c_{\text{vir}}$  found among lensing clusters. Here we compare our results with theoretical predictions based on the  $\Lambda$ CDM model.

For the theoretical prediction, we adopt results of  $N$ -body simulations in the Wilkinson Microwave Anisotropy Probe (WMAP) 5-year cosmology (Duffy et al. 2008). They derived the mean concentration of dark halos as a function of halo mass and redshift as

$$\bar{c}_{\text{vir}}(\text{sim}) = \frac{7.85}{(1+z)^{0.71}} \left( \frac{M_{\text{vir}}}{2.78 \times 10^{12} M_{\odot}} \right)^{-0.081}. \quad (17)$$

The apparent concentration parameters for halos with given mass and redshift are significantly scattered, with approximately the log-normal distribution with  $\sigma_{\log c} \simeq 0.14$ . However, the diversity of the halo population found in  $N$ -body simulations suggest that clusters with giant arcs should represent a quite biased population. This lensing bias arises from the fact that the lensing cross section is a sensitive function of the halo concentration. Therefore we



expect projected mass distributions of lensing clusters to be more centrally concentrated than ordinary clusters, implying that the clusters are intrinsically more concentrated and/or their major axes are preferentially aligned with the line-of-sight. Hennawi et al. (2007) estimated the lensing clusters have  $\sim 40\%$  higher values of concentrations compared with normal clusters (see also Fedeli et al. 2007). Oguri & Blandford (2009) focused on clusters with larger Einstein radii and argued that such clusters have  $\sim 40 - 60\%$  higher concentrations. Based on these discussions, in this paper we consider 50% enhancement of  $c_{\text{vir}}$  due to the lensing bias. From the calculation of Oguri & Blandford (2009), it is also found that the apparent concentration of the lensing clusters has slightly smaller scatter with  $\sigma_{\log c} \simeq 0.12$ .

Figure 8 shows the distribution of  $c_{\text{vir}}$  of the four clusters we study in this paper as well as several lensing clusters studied before. We consider only clusters whose radial profiles are well constrained from combined strong and weak lensing analyses. We find that all the four clusters have best-fit value of  $c_{\text{vir}}$  higher than the theoretical expectations. We still see the excess even if we take the lensing bias into account, although the value of  $c_{\text{vir}}$  for each cluster is marginally consistent with the theory if the error is taken into account. Put another way, the excess is not so strong as claimed in earlier work based on analysis of different lensing clusters (Broadhurst et al. 2005a, 2008; Comerford & Natarajan 2007). By combining all the 10 clusters, it is clear that our sample of lensing clusters has larger concentrations than expected from the  $M_{\text{vir}}-c_{\text{vir}}$  relation predicted by the  $\Lambda$ CDM model. The concentrations are also higher than the relation determined observationally by Comerford & Natarajan (2007) for a sample of lensing and X-ray clusters. Since our sample cannot constrain the redshift and mass dependence of the mean concentration very well, we fix them to those in equation (17) and fit the overall normalization to the data. We find

$$\bar{c}_{\text{vir}}(\text{fit}) = \frac{12.4}{(1+z)^{0.71}} \left( \frac{M_{\text{vir}}}{10^{15} M_{\odot}} \right)^{-0.081}, \quad (18)$$

as our best-fit to the results of 10 lensing clusters. The data are inconsistent with the concentration parameter predicted in the  $\Lambda$ CDM by  $7\sigma$ , even if we include the 50% enhancement to account for the lensing bias. A simple average of the concentration parameter (with the inverse of the measurement error as a weight) ignoring the mass and redshift dependence is  $\langle c_{\text{vir}} \rangle = 9.3 \pm 2.6$ .

We also check the excess as a function of the Einstein radius, which is a central quantity to characterize the central structure of a cluster (e.g., Broadhurst & Barkana 2008). The plot in Figure 8 shows that the excess of  $c_{\text{vir}}$  depends slightly on the Einstein radius. We fit the data by a power-law and find

$$\frac{\bar{c}_{\text{vir}}(\text{fit})}{\bar{c}_{\text{vir}}(\text{sim})} = 2.4 \left( \frac{\theta_{\text{Ein}}}{35''} \right)^{0.41}, \quad (19)$$

where  $\theta_{\text{Ein}}$  is the Einstein radius for the source redshift  $z_s = 3$ . The hypothesis that this ratio does not depend on the Einstein radius is rejected at 99% confidence level. The weak dependence of the excess on the Einstein radius is reasonable in the sense that concentrated two-dimensional mass distributions are required for clusters to produce large Einstein radii (e.g., Broadhurst et al. 2008; Oguri & Blandford 2009).

## 6. Summary and Discussion

In this paper, we have studied the mass profiles of four clusters by combining strong lens constraints with weak lensing shear measurements. We have drawn our sample from giant arc clusters newly discovered by the SGAS, the new arc survey using the SDSS data (Hennawi et al. 2008). We take advantage of follow-up wide-field *Subaru* Suprime-cam images to obtain weak lensing constraints out to nearly the virial radii of the clusters. The central densities of the clusters are determined well from the arcs with the redshifts spectroscopically measured partly from our ongoing program with the *Gemini* telescope. The technique allows us to study the radial mass profile over 2 dex in radius, which is essential for reliable extractions of concentrations of the clusters.

We have found that the radial profiles are fitted well by the NFW profile. We have determined the virial mass  $M_{\text{vir}}$  and concentration parameter  $c_{\text{vir}}$  of the four clusters accurately from the combined strong and weak lensing analysis. We confirmed that strongly lensed background galaxies with measured redshifts indeed improve constraints on mass profiles, particularly  $c_{\text{vir}}$ . We have found the values of  $c_{\text{vir}}$  for our 4 clusters to be  $c_{\text{vir}} \sim 8$ , except for SDSS2111 whose radial profile was not constrained very well because of insufficient strong lens information. The values are slightly higher than the  $\Lambda$ CDM predictions, even if we take account of the lensing bias that clusters with giant arcs are more centrally concentrated than normal clusters, although the excess is not as large as that claimed in earlier work. By combining all the 10 clusters with strong plus weak lensing analysis available, we confirm a  $7\sigma$  excess of the concentration parameter compared with the  $\Lambda$ CDM prediction. We find that the excess is dependent on the Einstein radius of the system such that clusters with larger Einstein radii show larger excess of the concentration parameters.

There are several possible explanations for the excess of the concentration parameter. One such explanation is the effect of baryons (e.g., Kazantzidis et al. 2004; Gnedin et al. 2004; Puchwein et al. 2005; Lin et al. 2006; Rozo et al. 2008). In particular, the adiabatic contraction associated with the baryon cooling can enhance the core density of dark matter and hence can increase the concentration of clusters. Another possibility is that theoretical predictions are not so accurate. In particular, the probability distribution of the concentra-

tion parameter for very massive halos ( $\gtrsim 10^{15} h^{-1} M_{\odot}$ ) and its redshift evolution has not been studied very much in  $N$ -body simulations, and thus our theoretical predictions inevitably rely on extrapolations from lower-mass halos. For example, it has been claimed that the redshift evolution of the concentrations of most massive halos may be different from that of less massive halos (e.g., Zhao et al. 2003). Thus it is important to perform many realizations of large box-size  $N$ -body simulations to improve the accuracy of theoretical predictions at the high mass end. A more exotic interpretation is that clusters form earlier than expected from the  $\Lambda$ CDM model, as the concentration is known to correlate with the formation epoch of the cluster (Wechsler et al. 2002). Such modification of the formation epoch can for instance be realized by considering early dark energy or primordial non-Gaussianity (e.g., Mathis et al. 2004; Sadeh et al. 2007; Sadeh & Rephaeli 2008; Oguri & Blandford 2009).

This paper has presented initial results of detailed studies for our unique sample of giant arc clusters (Hennawi et al. 2008). To investigate the structure of lensing clusters in a more systematic and statistical manner, it is of great importance to extend this research by applying the technique we have developed in this paper to other lensing clusters. In addition, it is important to improve constraints on the mass models of individual clusters by adding more data. Measuring redshifts of more arcs will significantly refine our strong lens modeling. In addition, dynamical information from the velocity dispersion measurement, as well as X-ray and Sunyaev-Zel’dovich signals, provide an important cross check of our mass models (e.g., Mahdavi et al. 2007; Lemze et al. 2008, 2009). We are planning these follow-up observations for our sample of giant arc clusters.

We thank Marceau Limousin and Johan Richard for useful correspondence regarding the cluster A1703, Tom Broadhurst, Keiichi Umetsu, Elinor Medezinski, Masahiro Takada, Nobuhiro Okabe, and Maruša Bradač for discussions on weak lensing, and Gilles Orban de Xivry, Phil Marshall, and Roger Blandford for bringing our attention to a higher-order catastrophe. This work was supported in part by Department of Energy contract DE-AC02-76SF00515. The authors wish to recognize and acknowledge the very significant cultural role and reverence that the summit of Mauna Kea has always had within the indigenous Hawaiian community. We are most fortunate to have the opportunity to conduct observations from this mountain.

## REFERENCES

Abraham, R. G., et al. 2004, *AJ*, 127, 2455

- Bardeau, S., Soucail, G., Kneib, J.-P., Czoske, O., Ebeling, H., Hudelot, P., Smail, I., & Smith, G. P. 2007, *A&A*, 470, 449
- Bernardi, M., et al. 2003, *AJ*, 125, 1849
- Bertin, E., & Arnouts, S. 1996, *A&AS*, 117, 393
- Bradač, M., et al. 2006, *ApJ*, 652, 937
- Bradač, M., et al. 2008a, *ApJ*, 681, 187
- Bradač, M., Allen, S. W., Treu, T., Ebeling, H., Massey, R., Morris, R. G., von der Linden, A., & Applegate, D. 2008b, *ApJ*, 687, 959
- Broadhurst, T., & Barkana, R. 2008, *MNRAS*, 390, 1647
- Broadhurst, T., Takada, M., Umetsu, K., Kong, X., Arimoto, N., Chiba, M., & Futamase, T. 2005a, *ApJ*, 619, L143
- Broadhurst, T., et al. 2005b, *ApJ*, 621, 53
- Broadhurst, T., Umetsu, K., Medezinski, E., Oguri, M., & Rephaeli, Y. 2008, *ApJ*, 685, L9
- Bullock, J. S., Kolatt, T. S., Sigad, Y., Somerville, R. S., Kravtsov, A. V., Klypin, A. A., Primack, J. R., & Dekel, A. 2001, *MNRAS*, 321, 559
- Clowe, D., & Schneider, P. 2001, *A&A*, 379, 384
- Comerford, J. M., & Natarajan, P. 2007, *MNRAS*, 379, 190
- Corless, V. L., & King, L. J. 2007, *MNRAS*, 380, 149
- Corless, V. L., King, L. J., & Clowe, D. 2009, *MNRAS*, accepted (arXiv:0812.0632)
- Deb, S., Goldberg, D. M., & Ramdass, V. J. 2008, *ApJ*, 687, 39
- Diego, J. M., Tegmark, M., Protopapas, P., & Sandvik, H. B. 2007, *MNRAS*, 375, 958
- Duffy, A. R., Schaye, J., Kay, S. T., & Dalla Vecchia, C. 2008, *MNRAS*, 390, L64
- Eisenstein, D. J., et al. 2005, *ApJ*, 633, 560
- Erben, T., Van Waerbeke, L., Bertin, E., Mellier, Y., & Schneider, P. 2001, *A&A*, 366, 717
- Fedeli, C., Bartelmann, M., Meneghetti, M., & Moscardini, L. 2007, *A&A*, 473, 715

- Gavazzi, R., Fort, B., Mellier, Y., Pelló, R., & Dantel-Fort, M. 2003, *A&A*, 403, 11
- Gavazzi, R. 2005, *A&A*, 443, 793
- Gladders, M. D., & Yee, H. K. C. 2000, *AJ*, 120, 2148
- Gladders, M. D., & Yee, H. K. C. 2005, *ApJS*, 157, 1
- Gladders, M. D., Yee, H. K. C., Majumdar, S., Barrientos, L. F., Hoekstra, H., Hall, P. B., & Infante, L. 2007, *ApJ*, 655, 128
- Glazebrook, K., & Bland-Hawthorn, J. 2001, *PASP*, 113, 197
- Gnedin, O. Y., Kravtsov, A. V., Klypin, A. A., & Nagai, D. 2004, *ApJ*, 616, 16
- Golse, G., & Kneib, J.-P. 2002, *A&A*, 390, 821
- Halkola, A., Seitz, S., & Pannella, M. 2006, *MNRAS*, 372, 1425
- Hamana, T., et al. 2003, *ApJ*, 597, 98
- Hennawi, J. F., Dalal, N., Bode, P., & Ostriker, J. P. 2007, *ApJ*, 654, 714
- Hennawi, J. F., et al. 2008, *AJ*, 135, 664
- Hetterscheidt, M., Simon, P., Schirmer, M., Hildebrandt, H., Schrabback, T., Erben, T., & Schneider, P. 2007, *A&A*, 468, 859
- Heymans, C., et al. 2006, *MNRAS*, 368, 1323
- Hicks, A. K., et al. 2007, *ApJ*, 671, 1446
- Hoekstra, H., Franx, M., & Kuijken, K. 2000, *ApJ*, 532, 88
- Hook, I. M., Jørgensen, I., Allington-Smith, J. R., Davies, R. L., Metcalfe, N., Murowinski, R. G., & Crampton, D. 2004, *PASP*, 116, 425
- Ilbert, O., et al. 2006, *A&A*, 457, 841
- Jaffe, W. 1983, *MNRAS*, 202, 995
- Jing, Y. P., & Suto, Y. 2000, *ApJ*, 529, L69
- Kaiser, N., & Squires, G. 1993, *ApJ*, 404, 441
- Kaiser, N., Squires, G., & Broadhurst, T. 1995, *ApJ*, 449, 460

- Kazantzidis, S., Kravtsov, A. V., Zentner, A. R., Allgood, B., Nagai, D., & Moore, B. 2004, *ApJ*, 611, L73
- Keeton, C. R. 2001, preprint (astro-ph/0102340)
- King, L. J., Clowe, D. I., & Schneider, P. 2002, *A&A*, 383, 118
- Kneib, J.-P., et al. 2003, *ApJ*, 598, 804
- Kochanek, C. S. 1991, *ApJ*, 373, 354
- Komatsu, E., et al. 2009, *ApJS*, in press (arXiv:0803.0547)
- Lemze, D., Barkana, R., Broadhurst, T. J., & Rephaeli, Y. 2008, *MNRAS*, 386, 1092
- Lemze, D., Broadhurst, T., Rephaeli, Y., Barkana, R., & Umetsu, K. 2009, *ApJ*, submitted (arXiv:0810.3129)
- Limousin, M., et al. 2007, *ApJ*, 668, 643
- Limousin, M., et al. 2008, *A&A*, 489, 23
- Lin, W. P., Jing, Y. P., Mao, S., Gao, L., & McCarthy, I. G. 2006, *ApJ*, 651, 636
- Maccio', A. V., Dutton, A. A., & van den Bosch, F. C. 2008, *MNRAS*, 391, 1940
- Mahdavi, A., Hoekstra, H., Babul, A., Sievers, J., Myers, S. T., & Henry, J. P. 2007, *ApJ*, 664, 162
- Massey, R., et al. 2007, *MNRAS*, 376, 13
- Mathis, H., Diego, J. M., & Silk, J. 2004, *MNRAS*, 353, 681
- McDonald, P., et al. 2005, *ApJ*, 635, 761
- Medezinski, E., et al. 2007, *ApJ*, 663, 717
- Meneghetti, M., Bartelmann, M., & Moscardini, L. 2003, *MNRAS*, 346, 67
- Merten, J., Cacciato, M., Meneghetti, M., Mignone, C., & Bartelmann, M. 2009, *A&A*, submitted (arXiv:0806.1967)
- Miyazaki, S., et al. 2002, *PASJ*, 54, 833
- Miyazaki, S., Hamana, T., Ellis, R. S., Kashikawa, N., Massey, R. J., Taylor, J., & Refregier, A. 2007, *ApJ*, 669, 714

- Natarajan, P., & Kneib, J.-P. 1997, MNRAS, 287, 833
- Natarajan, P., Kneib, J.-P., Smail, I., & Ellis, R. S. 1998, ApJ, 499, 600
- Natarajan, P., Kneib, J.-P., & Smail, I. 2002, ApJ, 580, L11
- Natarajan, P., Kneib, J.-P., Smail, I., Treu, T., Ellis, R., Moran, S., Limousin, M., & Czoske, O. 2009, ApJ, in press (arXiv:0711.4587)
- Navarro, J. F., Frenk, C. S., & White, S. D. M. 1997, ApJ, 490, 493
- Neto, A. F., et al. 2007, MNRAS, 381, 1450
- Oguri, M., & Blandford, R. D. 2009, MNRAS, 392, 930
- Oguri, M., Takada, M., Umetsu, K., & Broadhurst, T. 2005, ApJ, 632, 841
- Okabe, N., & Umetsu, K. 2008, PASJ, 60, 345
- Ouchi, M., et al. 2004, ApJ, 611, 660
- Puchwein, E., Bartelmann, M., Dolag, K., & Meneghetti, M. 2005, A&A, 442, 405
- Richard, J., Pei, L., Limousin, M., Jullo, E., & Kneib, J.-P. 2009, arXiv:0901.0427
- Rozo, E., Nagai, D., Keeton, C., & Kravtsov, A. 2008, ApJ, 687, 22
- Saha, P., & Read, J. I. 2009, ApJ, 690, 154
- Sand, D. J., Treu, T., Ellis, R. S., Smith, G. P., & Kneib, J.-P. 2008, ApJ, 674, 711
- Schramm, T. 1990, A&A, 231, 19
- Umetsu, K., & Broadhurst, T. 2008, ApJ, 684, 177
- Umetsu, K., et al. 2009, ApJ, in press (arXiv:0810.0969)
- Sadeh, S., Rephaeli, Y., & Silk, J. 2007, MNRAS, 380, 637
- Sadeh, S., & Rephaeli, Y. 2008, MNRAS, 388, 1759
- Schlegel, D. J., Finkbeiner, D. P., & Davis, M. 1998, ApJ, 500, 525
- Seitz, C., & Schneider, P. 1997, A&A, 318, 687
- Spergel, D. N., et al. 2003, ApJS, 148, 175

Vikhlinin, A., et al. 2009, ApJ, in press (arXiv:0812.2720)

Wambsganss, J., Ostriker, J. P., & Bode, P. 2008, ApJ, 676, 753

Wechsler, R. H., Bullock, J. S., Primack, J. R., Kravtsov, A. V., & Dekel, A. 2002, ApJ, 568, 52

Yagi, M., Kashikawa, N., Sekiguchi, M., Doi, M., Yasuda, N., Shimasaku, K., & Okamura, S. 2002, AJ, 123, 66

York, D. G., et al. 2000, AJ, 120, 1579

Zhao, D. H., Jing, Y. P., Mo, H. J., Boerner, G. 2003, ApJ, 597, L9



### A. Strong Lensing Modeling of A1703 by a Generalized NFW Profile

The multiple strong lens systems in A1703 for a wide range of source redshifts constrain enclosing masses at different radii. Thus we expect the dark matter density profile of this cluster can well be constrained (Limousin et al. 2008). By using the technique described in §3, we re-perform strong lens modeling of A1703 with the dark matter distribution replaced from equation (1) to a so-called generalized NFW profile (e.g., Jing & Suto 2000):

$$\rho(r) = \frac{\rho_s}{(r/r_s)^\alpha (1 + r/r_s)^{3-\alpha}}, \quad (\text{A1})$$

where  $\alpha = 1$  represent the original NFW profile. In Figure 9, we show the probability distribution of  $\alpha$  obtained from mass modeling. The result,  $\alpha = 0.9_{-0.4}^{+0.2}$ , is consistent with NFW, suggesting the validity of our assumption of  $\alpha = 1$  in our strong lens modeling in §3. An inner slope as steep as  $\alpha = 1.5$  is clearly rejected. The result is quite consistent with the recent strong lens modeling of A1703 by Richard et al. (2009),  $\alpha = 0.92_{-0.04}^{+0.05}$ , but with much larger error. It is not clear why our constraint on  $\alpha$  is much weaker than that of Richard et al. (2009); one of the reasons may be that we are conservatively using only spectroscopically confirmed, robustly identified multiple images for our mass modeling. We note that an inner slope slightly shallower than NFW was suggested in some other lensing clusters as well (Sand et al. 2008).

Table 1. Summary of *Subaru* Suprime-cam images

| Name     | Band     | Exposure<br>[sec] | Seeing<br>[arcsec] | $m_{\text{lim}}$ |
|----------|----------|-------------------|--------------------|------------------|
| A1703    | <i>g</i> | 400×3             | 0.96               | 26.39            |
|          | <i>r</i> | 300×7             | 0.80               | 26.31            |
|          | <i>i</i> | 240×5             | 0.86               | 25.58            |
| SDSS1446 | <i>g</i> | 400×3             | 0.84               | 26.22            |
|          | <i>r</i> | 300×7             | 0.82               | 26.24            |
|          | <i>i</i> | 240×5             | 0.92               | 25.47            |
| SDSS1531 | <i>g</i> | 400×3             | 0.90               | 26.28            |
|          | <i>r</i> | 300×5             | 0.98               | 26.19            |
|          | <i>i</i> | 240×5             | 1.00               | 25.38            |
| SDSS2111 | <i>g</i> | 360×4             | 0.82               | 26.13            |
|          | <i>r</i> | 300×8             | 0.60               | 26.05            |
|          | <i>i</i> | 240×7             | 0.52               | 25.48            |

Note. — The seeing indicates the FWHM in the co-added mosaic image. The magnitude limit  $m_{\text{lim}}$  refers to the  $5\sigma$  detection limit of point sources for  $2''$  aperture diameter. In stacking SDSS1531 *r*-band and SDSS2111 *r*-band images, we removed a few frames with bad seeing values; these are excluded from the numbers of frames indicated in this Table.

Table 2. Multiple images for strong lens modeling

| Name     | Image | $\Delta x$<br>[arcsec] | $\Delta y$<br>[arcsec] | $\Delta r$<br>[arcsec] | Redshift |
|----------|-------|------------------------|------------------------|------------------------|----------|
| A1703    | A1    | −11.7                  | 6.8                    | 13.5                   | 0.8889   |
|          | A2    | −6.3                   | 8.4                    | 10.4                   |          |
|          | A3    | −4.8                   | 2.6                    | 5.3                    |          |
|          | A4    | −10.5                  | 0.8                    | 10.7                   |          |
|          | A5    | 22.1                   | −14.9                  | 26.7                   |          |
|          | B1    | −33.6                  | −11.6                  | 35.5                   | 2.627    |
|          | B2    | −25.7                  | −21.9                  | 33.8                   |          |
|          | B3    | 21.3                   | −28.5                  | 35.6                   |          |
|          | C1    | −32.3                  | −15.3                  | 35.7                   | 2.627    |
|          | C2    | −30.4                  | −18.0                  | 35.3                   |          |
|          | C3    | 21.3                   | −28.5                  | 35.6                   |          |
|          | D1    | 14.1                   | 32.7                   | 35.6                   | 1.908    |
|          | D2    | 25.0                   | 26.7                   | 36.6                   |          |
|          | D3    | −10.4                  | 37.8                   | 39.2                   |          |
|          | E1    | −17.5                  | 32.2                   | 36.6                   | 2.360    |
|          | E2    | 6.9                    | 30.0                   | 30.8                   |          |
| E3       | 34.4  | 7.2                    | 35.1                   |                        |          |
| F1       | 20.4  | −18.0                  | 27.2                   | 2.355                  |          |
| F2       | 11.0  | 13.8                   | 17.6                   |                        |          |
| F3       | −36.1 | 15.5                   | 39.3                   |                        |          |
| F4       | −7.1  | −21.3                  | 22.5                   |                        |          |
| SDSS1446 | A1    | −11.9                  | 14.9                   | 19.1                   | > 1.6    |
|          | A2    | 13.2                   | 11.6                   | 17.6                   |          |
|          | A3    | −4.9                   | −10.7                  | 11.8                   |          |
|          | A4    | 18.9                   | −5.3                   | 19.6                   |          |
| SDSS1531 | A1    | −11.5                  | 9.7                    | 15.0                   | 1.096    |
|          | A2    | 3.0                    | −10.5                  | 10.9                   |          |
|          | A3    | 4.4                    | −10.1                  | 11.0                   |          |
|          | A4    | 11.1                   | −0.6                   | 11.1                   |          |
|          | B1    | −13.3                  | 5.7                    | 14.5                   | 1.095    |

Table 2—Continued

| Name     | Image | $\Delta x$<br>[arcsec] | $\Delta y$<br>[arcsec] | $\Delta r$<br>[arcsec] | Redshift |
|----------|-------|------------------------|------------------------|------------------------|----------|
| SDSS2111 | B2    | 6.8                    | 3.8                    | 7.8                    |          |
|          | A1    | 10.0                   | −5.1                   | 11.2                   | ...      |
|          | A2    | 6.1                    | −8.0                   | 10.1                   |          |
|          | A3    | −13.6                  | −8.9                   | 16.3                   |          |
|          | B1    | 8.6                    | −6.2                   | 10.6                   | ...      |
|          | B2    | 8.1                    | −7.1                   | 10.8                   |          |
|          | B3    | −16.3                  | −6.8                   | 17.7                   |          |
|          | C1    | 12.9                   | −4.5                   | 13.7                   | ...      |
|          | C2    | −0.1                   | −11.1                  | 11.1                   |          |
| C3       | −11.6 | −9.9                   | 15.3                   |                        |          |

Note. — The same alphabet of images indicates that they are associated with the same source, inferred based on the colors and modeling.  $\Delta x$  and  $\Delta y$  denote the relative locations from the BCG of each cluster (see Figure 1); the positive directions correspond to West and North, respectively. The distance from the BCG is shown as  $\Delta r$ . Redshifts are spectroscopic redshifts (see text for more details). The arc identification and spectroscopic redshifts for A1703 are taken from Limousin et al. (2008) and Richard et al. (2009).

Table 3. Result of strong lens mass modeling

| Name     | $M_{\text{vir}}$<br>[ $10^{15} M_{\odot}$ ] | $x_c$<br>[arcsec]   | $y_c$<br>[arcsec]    | $e$                    | $\theta_e$<br>[deg]    | $c_{\text{vir}}$       | $\sigma$<br>[km s $^{-1}$ ] | $r_{\text{cut}}$<br>[arcsec] | $\chi^2/\text{dof}$ |
|----------|---|---------------------|----------------------|------------------------|------------------------|------------------------|-----------------------------|------------------------------|---------------------|
| A1703    | $2.41^{+0.70}_{-0.58}$                      | $-1.5 \pm 0.5$      | $0.7^{+0.5}_{-0.6}$  | $0.36^{+0.04}_{-0.03}$ | $-24.1^{+0.6}_{-0.7}$  | $5.1 \pm 0.7$          | $337^{+34}_{-36}$           | $14.9 \pm 3.6$               | 35.5/24             |
| SDSS1446 | $0.53^{+1.34}_{-0.28}$                      | $1.1^{+1.4}_{-1.6}$ | $-0.7^{+1.9}_{-2.9}$ | $0.42^{+0.44}_{-0.24}$ | $-36.3^{+2.0}_{-2.3}$  | $11.7^{+28.3}_{-7.2}$  | $231 \pm 38$                | $4.3^{+1.9}_{-2.0}$          | 0.0/0               |
| SDSS1531 | $4.39^{+2.61}_{-4.25}$                      | $0.4^{+1.8}_{-0.5}$ | $-0.8^{+0.3}_{-1.0}$ | $0.10^{+0.41}_{-0.04}$ | $-42.2^{+7.7}_{-3.7}$  | $3.0^{+13.0}_{-0.7}$   | $291^{+33}_{-24}$           | $8.4^{+2.9}_{-2.2}$          | 0.7/2               |
| SDSS2111 | $0.55^{+1.30}_{-0.27}$                      | $-3.9 \pm 1.5$      | $13.3^{+3.9}_{-5.9}$ | $0.45^{+0.27}_{-0.26}$ | $-168.2^{+2.7}_{-2.3}$ | $16.0^{+24.0}_{-10.1}$ | $268^{+51}_{-49}$           | $4.7^{+2.6}_{-2.4}$          | 1.5/6               |

Note. — The parameters  $x_c$  and  $y_c$  denote the center of a dark halo (NFW) component relative to the location of the BCG; positive  $x_c$  and  $y_c$  indicate the offset to West and North directions, respectively. The position angle  $\theta_e$  is East of North. The values of the velocity dispersion  $\sigma$  and the cutoff radius  $r_{\text{cut}}$  in this table are those of the BCG; other member galaxies have values obtained from the exact scaling relation  $\sigma \propto L^{1/4}$  and  $r_{\text{cut}} \propto L^{1/2}$ . Note that we have assumed the arc redshifts of SDSS1446 and SDSS2111 to be  $z = 1.6$  when running the MCMC; some of the best-fit values (e.g.,  $M_{\text{vir}}$ ) is dependent on this assumption.

Table 4. Einstein radii from strong lens mass modeling

| Name     | $\theta_{\text{Ein}}$ [arcsec] | $z_{\text{Ein}}$ |
|----------|--------------------------------|------------------|
| A1703    | $12.1^{+1.6}_{-1.3}$           | 0.8889           |
|          | $22.5^{+1.8}_{-1.7}$           | 2.627            |
| SDSS1446 | $16.5^{+4.7}_{-1.8}$           | 1.6 – 3.5        |
| SDSS1531 | $9.3^{+2.9}_{-0.8}$            | 1.096            |
| SDSS2111 | $18.6^{+4.4}_{-5.3}$           | < 3.5            |

Note. — The Einstein radius  $\theta_{\text{Ein}}$  is that predicted by the best-fit dark halo component, i.e., contributions from member galaxies (including the BCGs) are excluded in deriving  $\theta_{\text{Ein}}$ . See text for more details.

Table 5. Ellipticities of template stars for the PSF correction

| Name     | $e_1^* \times 10^2$ | $e_2^* \times 10^2$ | $e_{1,\text{cor}}^* \times 10^2$ | $e_{2,\text{cor}}^* \times 10^2$ | $N_{\text{star}}$ |
|----------|---------------------|---------------------|----------------------------------|----------------------------------|-------------------|
| A1703    | $+0.88 \pm 1.11$    | $+0.56 \pm 1.22$    | $-0.02 \pm 0.49$                 | $-0.01 \pm 0.43$                 | 558               |
| SDSS1446 | $-1.08 \pm 0.82$    | $-0.35 \pm 0.76$    | $-0.01 \pm 0.45$                 | $-0.02 \pm 0.34$                 | 598               |
| SDSS1531 | $+0.79 \pm 0.94$    | $+0.14 \pm 0.85$    | $-0.01 \pm 0.45$                 | $+0.00 \pm 0.39$                 | 876               |
| SDSS2111 | $-0.87 \pm 1.82$    | $-1.60 \pm 1.22$    | $-0.01 \pm 0.70$                 | $+0.03 \pm 0.44$                 | 1591              |

Note. — Medians and standard deviations of ellipticities for template stars used to correct PSF anisotropies.  $e^*$  and  $e_{\text{cor}}^*$  are ellipticities before and after the PSF correction. The last column shows the number of the template stars.

Table 6. Source galaxy population for weak lensing analysis

| Name     | $z_l$ | Magnitude         | $\langle d_{ls}/d_{os} \rangle$ | $z_d$ | $N_{\text{gal}}$ |
|----------|-------|-------------------|---------------------------------|-------|------------------|
| A1703    | 0.281 | $22.0 < r < 25.7$ | 0.637                           | 0.899 | 9155             |
| SDSS1446 | 0.464 | $22.0 < r < 25.3$ | 0.470                           | 0.999 | 9985             |
| SDSS1531 | 0.335 | $22.0 < r < 24.9$ | 0.546                           | 0.832 | 6032             |
| SDSS2111 | 0.637 | $22.0 < r < 26.0$ | 0.383                           | 1.181 | 9721             |

Note. — The range of  $r$ -band magnitudes, lensing depth  $\langle d_{ls}/d_{os} \rangle$ , effective source redshifts  $z_d$ , and the numbers of source galaxies  $N_{\text{gal}}$  are shown. See text for details.

Table 7. Result from weak lensing and combined strong and weak lensing analysis

| Name     | Weak lensing                        |                       |                     | Strong and weak lensing             |                       |                     |
|----------|-------------------------------------|-----------------------|---------------------|-------------------------------------|-----------------------|---------------------|
|          | $M_{\text{vir}}[10^{15} M_{\odot}]$ | $c_{\text{vir}}$      | $\chi^2/\text{dof}$ | $M_{\text{vir}}[10^{15} M_{\odot}]$ | $c_{\text{vir}}$      | $\chi^2/\text{dof}$ |
| A1703    | $1.95^{+0.65}_{-0.50}$              | $3.3^{+1.4}_{-1.1}$   | 2.7/5               | $1.50^{+0.40}_{-0.35}$              | $6.5^{+1.2}_{-0.7}$   | 7.9/7               |
| SDSS1446 | $0.83^{+0.29}_{-0.25}$              | $9.1^{+11.4}_{-4.1}$  | 6.3/5               | $0.83^{+0.30}_{-0.22}$              | $8.3^{+3.9}_{-3.1}$   | 6.4/6               |
| SDSS1531 | $0.59^{+0.39}_{-0.26}$              | $11.5^{+28.5}_{-7.4}$ | 8.0/5               | $0.66^{+0.29}_{-0.24}$              | $7.9^{+3.0}_{-1.5}$   | 8.1/6               |
| SDSS2111 | $0.92^{+0.41}_{-0.32}$              | $14.1^{+25.9}_{-9.5}$ | 7.5/5               | $0.92^{+0.41}_{-0.32}$              | $14.1^{+25.9}_{-9.3}$ | 7.5/6               |

Note. — Weak lensing constraints come from radial profiles of tangential shear  $g_+$  (see Figure 5). The Einstein radii  $\theta_{\text{Ein}}$  inferred from strong lens modeling are used as strong lens constraints (see Table 4). Note that we have restricted the range of the concentration parameter to  $c_{\text{vir}} < 40$ . The virial radii of the best-fit models from strong and weak lensing analysis are 2.56, 1.91, 1.89, and 1.80 Mpc for A1703, SDSS1446, SDSS1531, and SDSS2111, respectively.

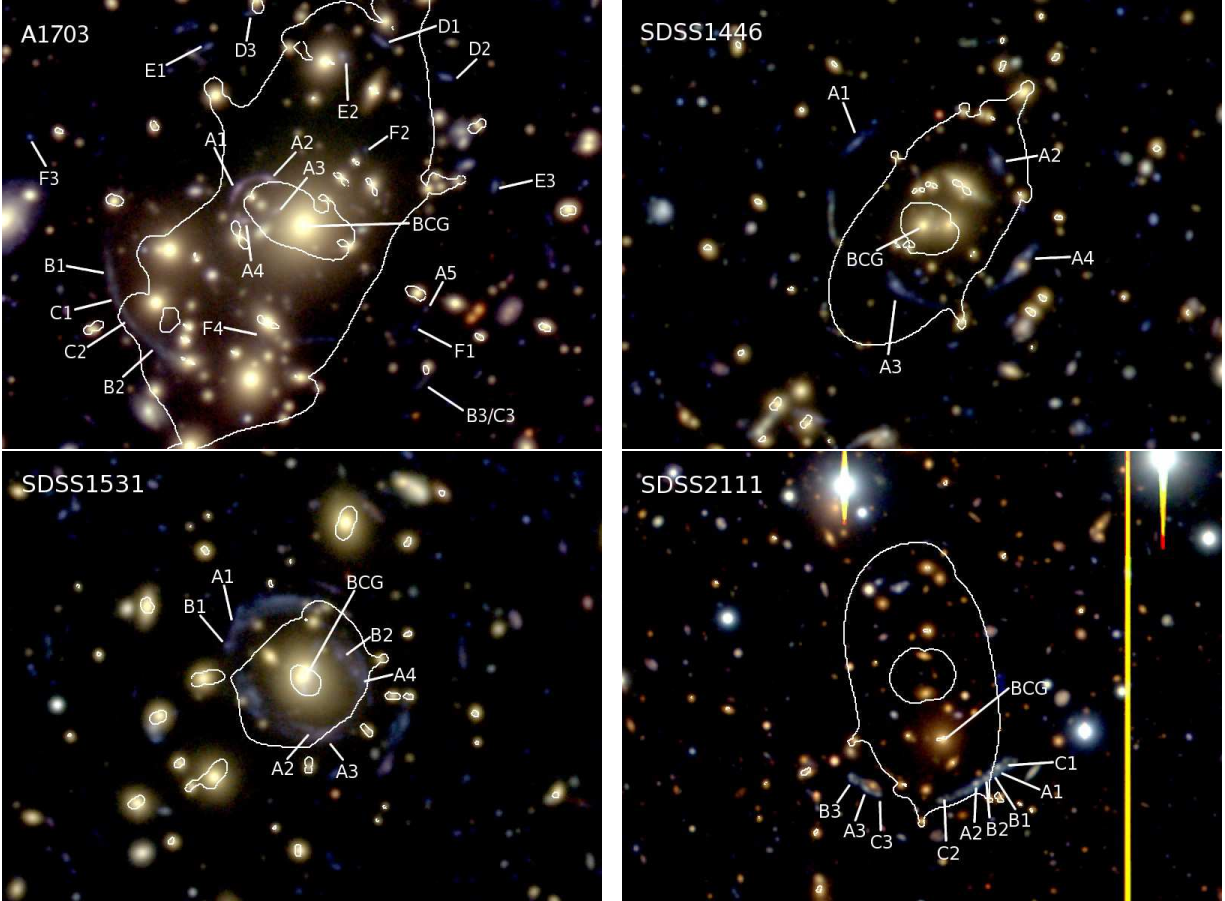


Fig. 1.— *Subaru* Suprime-cam images of 4 clusters we study in this paper. North is up and East is left. The size of each image is  $107'' \times 80''$ . Multiple images we adopt for strong lens modeling are named by an alphabet and a number (e.g., A1; see also Table 2). Critical curves of our best-fit models at the redshifts of multiple images ( $z = 2.627$  for A1703) are drawn by solid lines (see §3.3). The brightest cluster galaxy for each cluster is marked by “BCG”. The J2000.0 coordinates of the BCGs are 13:15:05.24+51:49:02.7 (A1703), 14:46:34.03+30:32:58.7 (SDSS1446), 15:31:10.63+34:14:24.9 (SDSS1531), and 21:11:19.36–01:14:22.9 (SDSS2111).



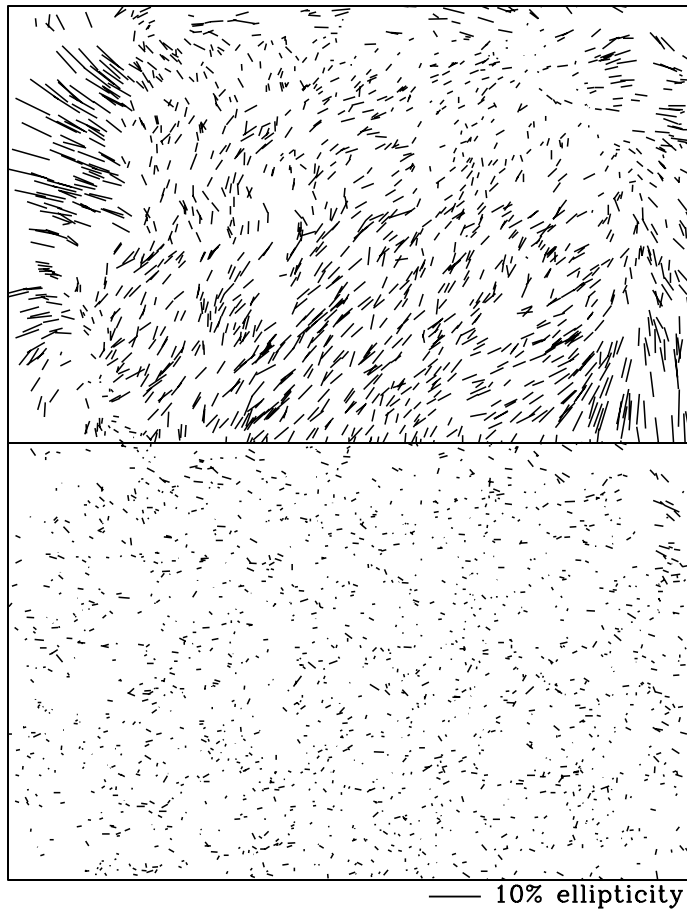


Fig. 2.— PSF anisotropy maps of the field of SDSS2111 measured from template stars. The upper panel shows the raw ellipticities of the stars, whereas the lower panel is stellar ellipticities after the PSF correction is applied. The length and orientation of each line segment indicates the ellipticity and position angle of each template star. The size of each panel is  $\sim 35'.5 \times 26'.5$ , i.e., the entire field of the mosaic image is shown here. Table 5 lists ellipticities before and after the PSF correction for the fields of all the clusters.

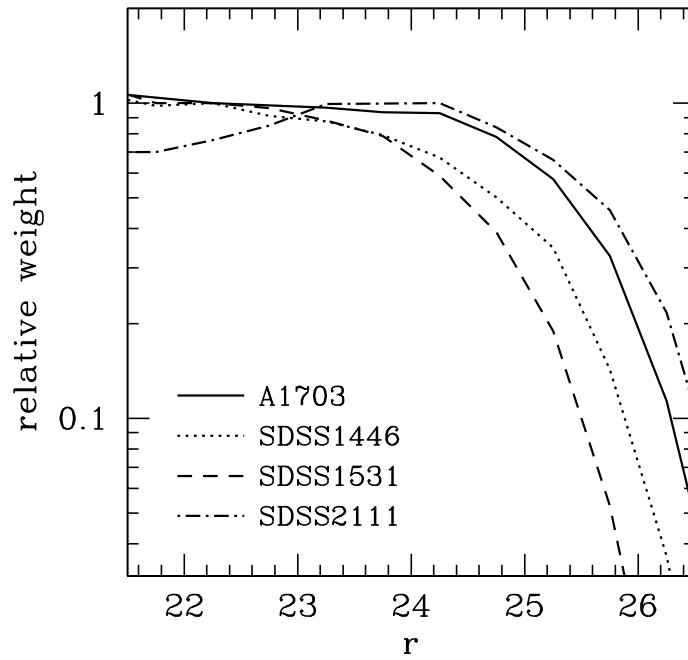


Fig. 3.— The relative weight  $w(r)$  of our background galaxy samples as a function of total  $r$ -band magnitudes, derived from the number ratio of source galaxies for weak lensing analysis and galaxies in the CFHTLS (Ilbert et al. 2006). The color cut  $g - i < 1.0$  is applied to both galaxy samples. The weights are normalized by the maximum weight at  $r > 22$ .

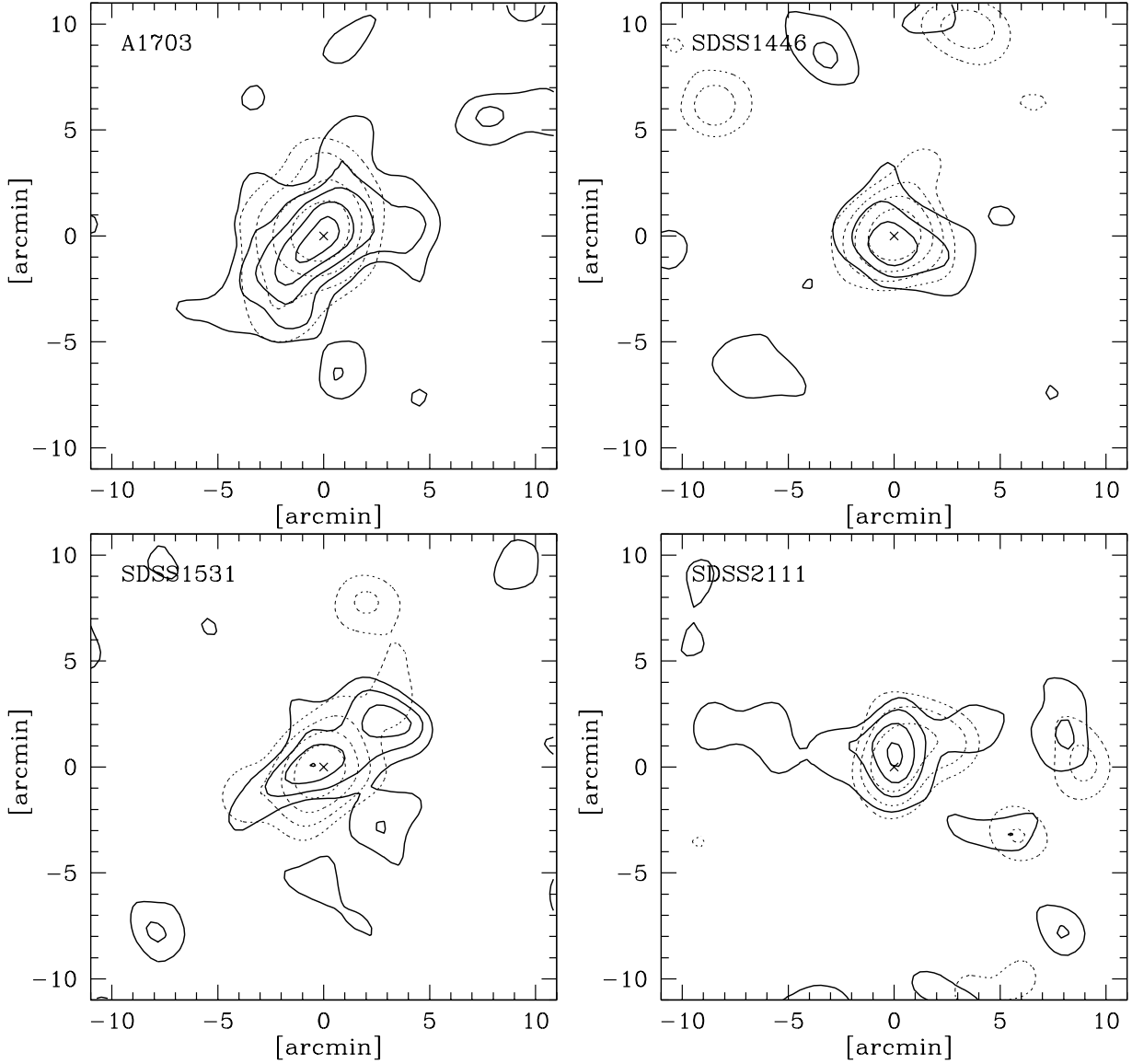


Fig. 4.— Two-dimensional mass maps (*solid*) reconstructed from weak lensing shear measurements. North is up and East is left. Contours are drawn with spacing of  $\Delta\kappa = 0.04$ , starting from  $\kappa = 0.04$ . Note that the  $1\sigma$  noise level of each reconstructed mass map is  $\sigma_\kappa \sim 0.03$ . Crosses indicate the locations of the BCGs. Contours of constant luminosity densities of red-sequence galaxies (*dotted*) are also shown for comparison. Both mass and luminosity maps are Gaussian-smoothed with  $\sigma = 60''$ .

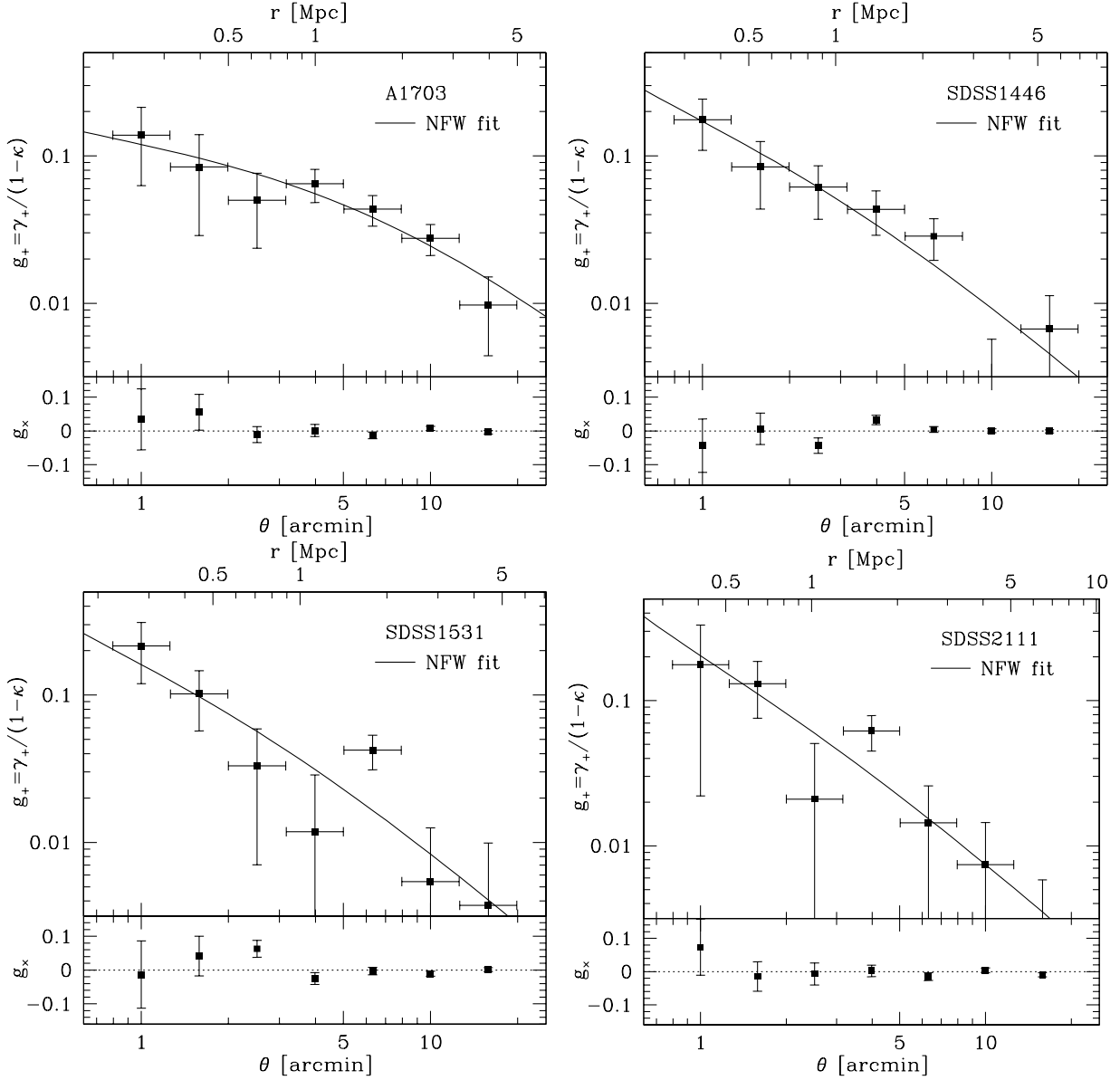


Fig. 5.— Azimuthally-averaged tangential shear  $g_+$  (eq. [11]) and the 45° rotated component  $g_x$  (eq. [12]) as a function of distance from the cluster center. The NFW models fitted to the observed shear profiles are shown by solid lines (see also Table 7).

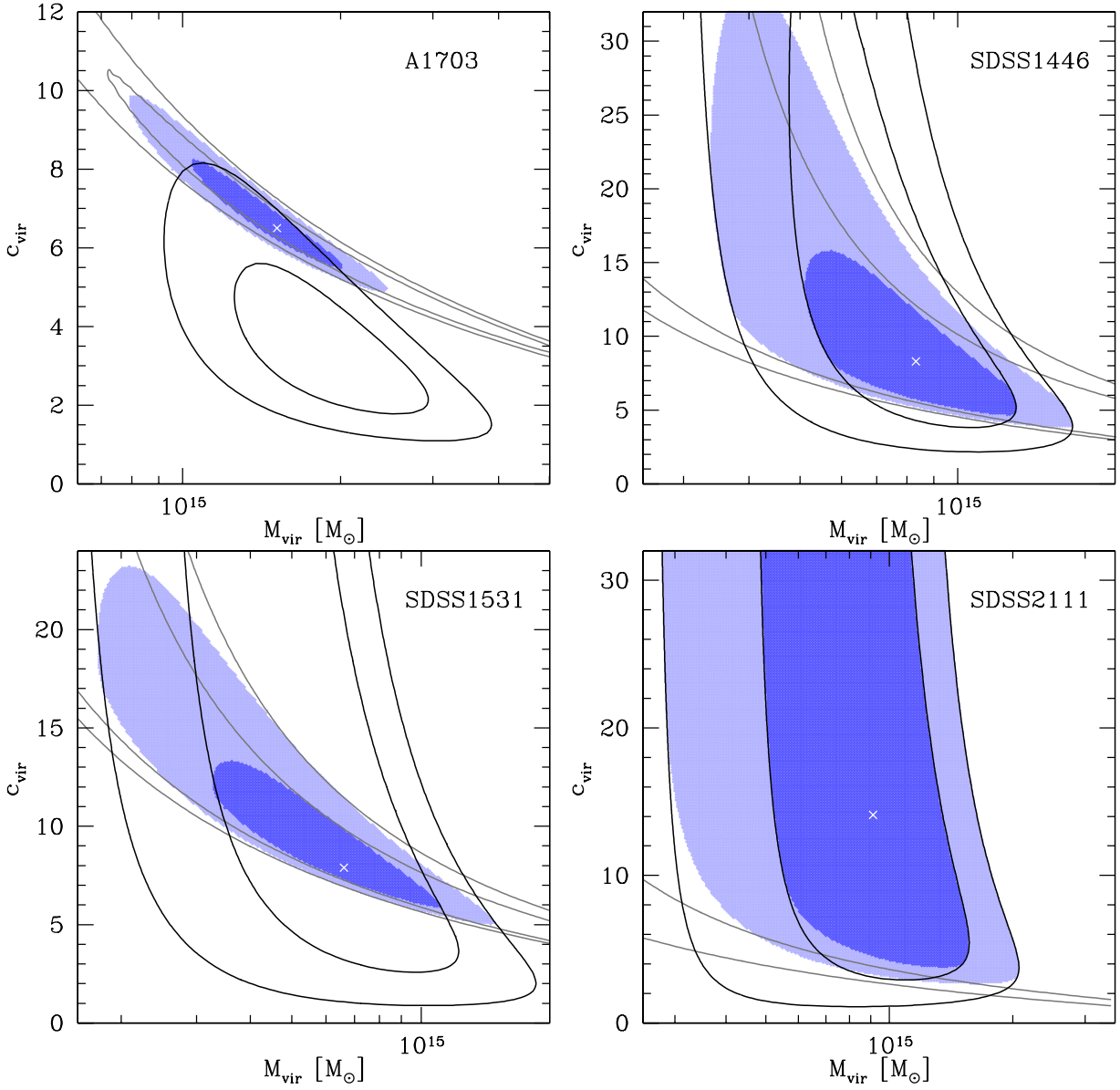


Fig. 6.— Contours at  $1\sigma$  and  $2\sigma$  confidence levels in the  $M_{\text{vir}}-c_{\text{vir}}$  plane. Black and grey lines indicate constraints from weak or strong lensing, respectively. Combined strong and weak lensing constraints are plotted by shaded regions. The best-fit model parameters from combined strong and weak lensing are shown by crosses (see also Table 7).

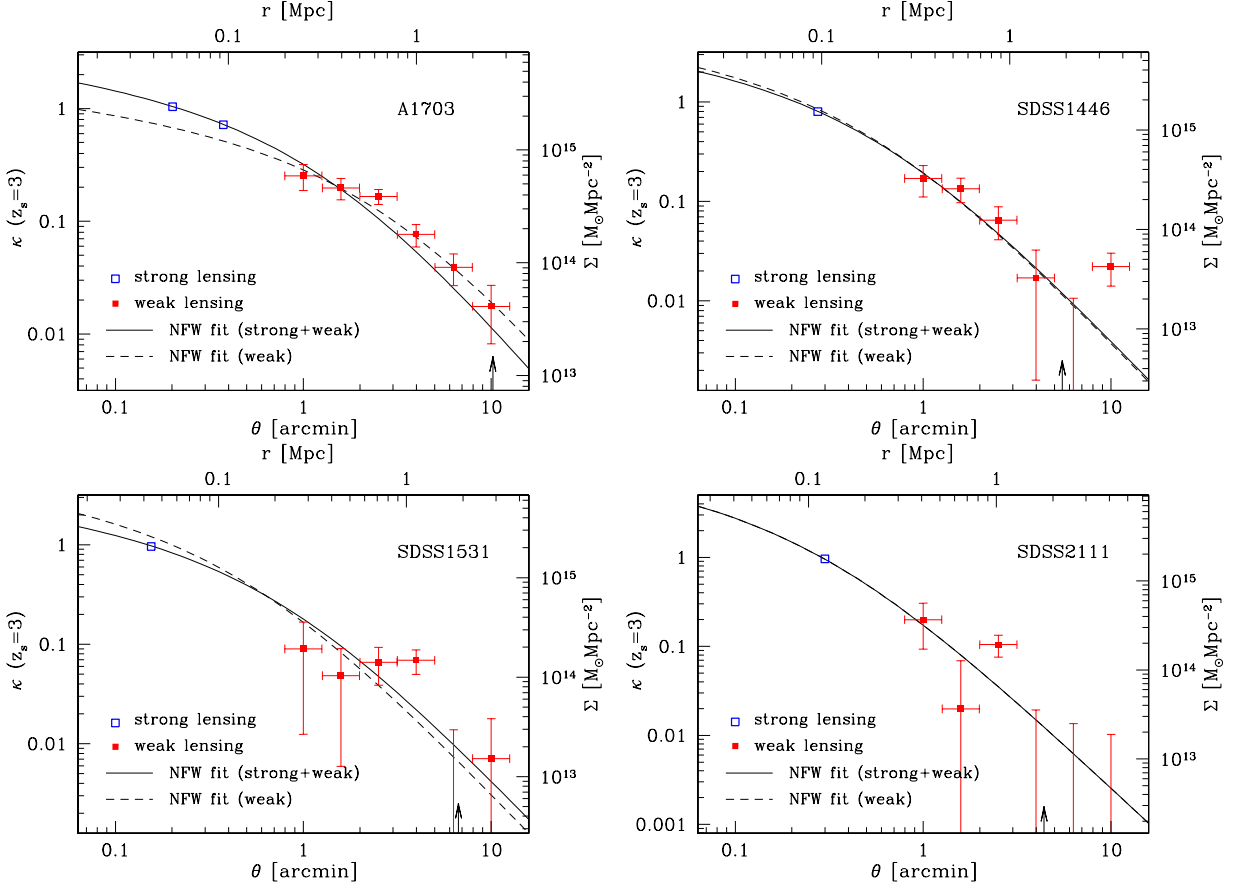


Fig. 7.— Radial profiles of convergence  $\kappa$  for the source redshift  $z_s = 3$  constrained from strong and weak lensing. Radial profiles of best-fit models from combined strong and weak lensing are plotted by solid lines, whereas those from weak lensing only are shown by dashed lines (see also Table 7). Filled squares are  $\kappa$  profiles reconstructed from weak lensing tangential shear profiles shown in Figure 5; as boundary conditions, we assumed values of convergences in the outermost radial bin to be those computed from the best-fit NFW profiles from weak lensing. We indicate the Einstein radii used as strong lens constraints by open squares, and the virial radii of the best-fit models from strong and weak lensing analysis by arrows.

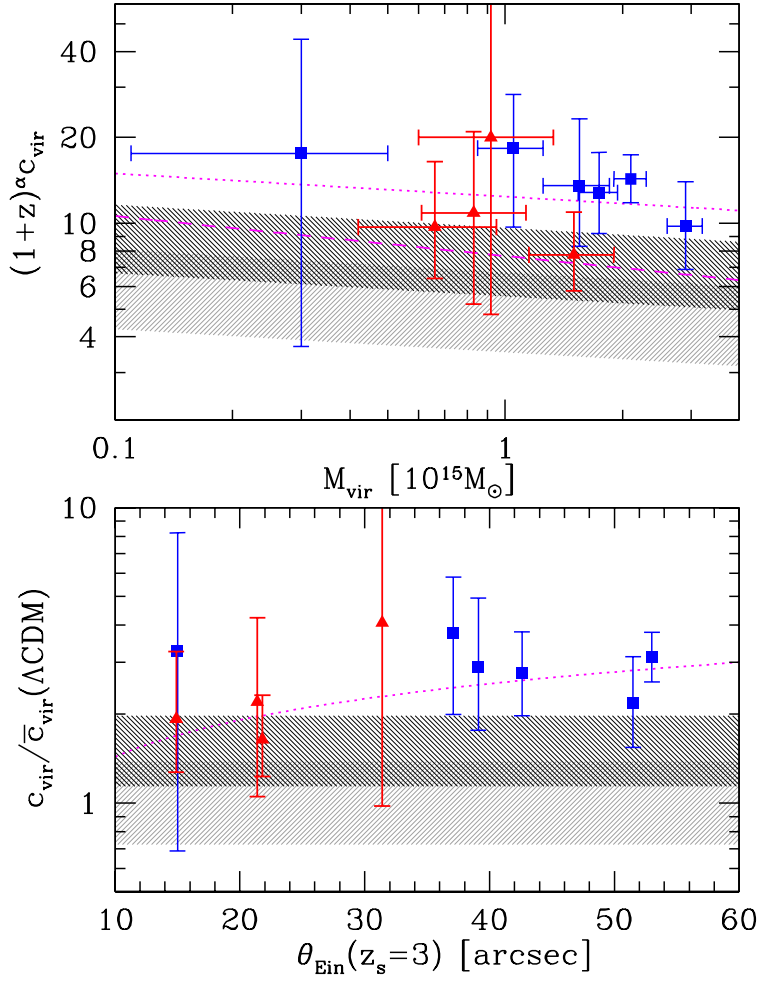


Fig. 8.— Distribution of the concentration parameter  $c_{\text{vir}}$  constrained from combined strong and weak lensing analysis. Filled triangles show our results presented in this paper, whereas filled squares are from literature, results for A1689 (Umetsu & Broadhurst 2008), A2261 (Umetsu et al. 2009), A370, RXJ1347, CL0024 (Broadhurst et al. 2008), and MS2137 (Gavazzi et al. 2003). *Upper:* The distribution of  $c_{\text{vir}}$  as a function of virial mass  $M_{\text{vir}}$ . The data points are corrected for the redshift evolution of the concentration parameter predicted in the  $\Lambda$ CDM model,  $c_{\text{vir}} \propto (1+z)^{-\alpha}$  with  $\alpha = 0.71$  (Duffy et al. 2008). The grey shaded regions indicate  $1\sigma$  range of  $c_{\text{vir}}$  derived from  $\Lambda$ CDM simulations by Duffy et al. (2008). Black shaded regions show predicted concentration parameters after approximately taking the lensing bias ( $\sim 50\%$ ) into account (Hennawi et al. 2007; Oguri & Blandford 2009). The dashed line plots the  $M_{\text{vir}}-c_{\text{vir}}$  relation determined observationally from a sample of lensing and X-ray clusters (Comerford & Natarajan 2007). The dotted line shows the best-fit curve to the data. *Lower:* The ratios of  $c_{\text{vir}}$  from analyses of lensing clusters to those expected in  $\Lambda$ CDM are plotted a function of the Einstein radius  $\theta_{\text{Ein}}$  for the source redshifts  $z_s = 3$ . Again, the shaded regions show  $1\sigma$  range expected in  $\Lambda$ CDM, with (*black*) and without (*grey*) the lensing bias. The best-fit curve by a power-law is shown by the dotted line.

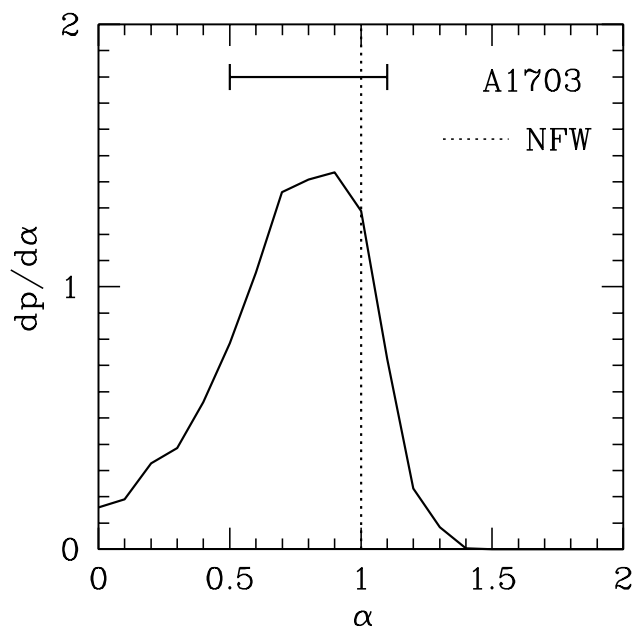


Fig. 9.— Normalized probability distribution of the inner slope of the dark matter density profile,  $\alpha$  (see eq. [A1]), from strong lens modeling of A1703. Other model parameters are marginalized over. The vertical dotted line indicates the slope of the original NFW profile ( $\alpha = 1$ ) which we assumed for analysis in §3. The horizontal bar denotes the  $1\sigma$  statistical error on  $\alpha$  derived from the probability distribution.